Tectonophysics 820 (2021) 229107

Contents lists available at ScienceDirect

Tectonophysics

journal homepage: www.elsevier.com/locate/tecto

Identifying geological structures through microseismic cluster and burst analyses complementing active seismic interpretation

A.M. Dichiarante [a,*], N. Langet [a], R.A. Bauer [b], B.P. Goertz-Allmann [a], S.C. Williams-Stroud [b], D. Kühn [a,c], V. Oye [a], S.E. Greenberg [b], B.D.E. Dando [a]

[a] NORSAR, Gunnar Randers Vei 15, 2007 Kjeller, Norway
[b] Illinois State Geological Survey, Champaign, IL, USA
[c] GFZ German Research Centre for Geosciences, Helmholtz Str. 6/7, 14467 Potsdam, Germany

ARTICLE INFO

Keywords:
Induced seismicity
Seismicity bursts
Fractures
Stress state
Basement

ABSTRACT

At the Decatur carbon capture and storage site (IL, USA) CO_2 has been injected from 2011–2014 and from 2017 to present near the base of the Lower Mt. Simon Sandstone saline reservoir, resulting in microseismicity. Microseismicity is mainly located in the basement and distributed in distinct spatial clusters. The lack of significant impedance contrasts within the basement makes the interpretation of active-source seismic reflection data challenging, however, recent reprocessing allowed to resolve faults above and at the top of the basement. These faults generally do not coincide with the location of microseismic events and their continuation to the general depth of the seismic events cannot be assumed. This paper shows how the interpretation of the microseismicity can complement structural interpretations of active-source seismic reflection data. In particular, we analyze clusters and bursts (abrupt increases) of microseismicity, identify unresolved, smaller-scale weaknesses and extract statistical parameters. These parameters allow comparisons with the interpreted faults, and with fracture sets intercepted by boreholes. During injection at the Decatur site, the injection pressure was kept far below fracture pressure, nevertheless, seismic events were induced and spread far beyond the expected extent of the CO_2 plume. We argue that local stress transfers related to the CO_2 injection reactivated pre-existing fractures within the critically stressed basement. Finally, we conducted a slip tendency analysis for faults interpreted from active seismic, selected cluster, bursts and nodal planes from focal mechanisms to determine if the interpreted structures are optimally oriented with respect to the stress regime. Our results suggest that the orientation of fractures close to the injection well, generally shows slight deviations from the optimal orientation for slip. This might indicate either slight local deviations of the maximum horizontal stress azimuth from the average direction used in the analysis, or the lack of optimally oriented fractures at this location.

1. Introduction

The injection of CO_2 into a reservoir causes direct changes in both the pore fluid pressure and in situ temperature due to the injected volume and temperature of CO_2. The pore-pressure changes occur mainly within the permeable reservoir. With time, both pressure and temperature changes can also dissipate into the low-permeable surrounding formations such as the caprock and underburden. The net change in pore-pressure due to injection (causing expansion) and thermal stresses from the cooling (causing contraction), deforms the reservoir and the surrounding formations. This deformation induces stress changes in magnitude and direction that are transferred far beyond the CO_2 plume and temperature footprint (Vilarrasa et al., 2013).

In most CO_2 storage projects, these stress changes are not large enough to create new fractures within the sealing caprock and surrounding intact rocks but they might be sufficient to reactivate pre-existing geological discontinuities and weaknesses (e.g., faults and associated fractures). These pre-existing structures, if penetrating a caprock, may be a possible leakage path for CO_2 and their identification is therefore crucial for risk assessment of storage integrity.

Monitoring has accompanied sequestration projects, allowing also for a better understanding of the subsurface (e.g., Furre et al., 2017; Verdon et al., 2010). Monitoring methodologies include: (i) monitoring of pressure and temperature at wells; (ii) active conventional

* Corresponding author.
E-mail address: anna.dichiarante@norsar.no (A.M. Dichiarante).

https://doi.org/10.1016/j.tecto.2021.229107
Received 16 July 2021; Received in revised form 29 September 2021; Accepted 6 October 2021
Available online 18 October 2021

geophysical methods (e.g., seismic reflection and gravimetric measurements) aimed to both ensure storage and injection feasibility and to investigate changes in the subsurface during and post injection; (iii) and microseismic monitoring to understand pre-injection background seismicity and induced or triggered seismicity during and post injection. These methodologies allow the evaluation of the geomechanical response of reservoir and surrounding regions.

Conventional active seismic methods are not able to detect faults with small vertical displacement or small discontinuities, due to resolution limits generally encountered in seismic imaging methods at large depths. The resolution limit is typically less than 10 m. Processing of 3D seismic reflection volumes for geometrical attributes, such as curvature, can sometimes illuminate subtle features that are related to discontinuities in the subsurface. For instance, at the In Salah CO_2 storage site at Krechba (Algeria), where injection pressures exceeded fracture pressure (Goertz-Allmann et al., 2014), a double-lobed displacement pattern indicating up to 20-mm ground surface uplift was measured using interferometric synthetic aperture radar (InSAR), but no structure was resolved through seismic imaging methods. The post-injection 3D seismic interpretation revealed a subtle "push-down structure" associated with linear features at depth below the double-lobed pattern, which was interpreted as a low-velocity zone due to the presence of CO_2. The calculation of ant-tracking attributes to extract trends from the data produced linear features that correlate well both with the low velocity zone and the displacement at the surface, and thus, were interpreted to represent an up to 3.5 km long sub-vertical fracture or damage zone (Zhang et al., 2015).

An increase in pore pressure reduces the effective stresses, shifting the stress state, often illustrated in a Mohr diagram, closer to or beyond the failure envelope of fractures and faults typically defined by the Coulomb criterion and friction coefficient, resulting in failure by shear slip or dilation (e.g., Sibson, 1985; Healy et al., 1968). The seismic energy released during such slip can be recorded by seismometers and geophones. The minimum moment magnitude Mw that may be detected by geophones is as low as −4 corresponding to an estimated slip of ca. 0.01 mm on a structure of ca. 3 cm radius (e.g., Fig. 2 in Zoback and Gorelick, 2012). Most commonly, the range of microseismic events is considered from Mw −3 to 0. To detect and locate small magnitude events, seismic instruments should be placed at short distances around the injector, within boreholes less than several hundred-meter distances and if at the surface within networks or arrays focusing on up to 1.5 times the injection depth.

The focus area of this paper is the Decatur (IL, USA) carbon capture and storage site (CCS), where CO_2 has been injected during two injection phases (Ph1 and Ph2) near the base of the Lower Mt. Simon Sandstone saline reservoir as part of two CCS projects (Finley, 2014; Williams-Stroud et al., 2020). During the first injection phase (Ph1), as part of the Illinois Basin – Decatur Project (IBDP), 1 million tonnes of CO_2 have been injected over a period of 3 years (November 2011–November 2014) into well CCS1 (well location in Fig. 1a). The second injection phase (Ph2), as part of the Illinois Industrial Carbon Capture and Sequestration (IL-ICCS), is ongoing since April 2017 and has permitted injection capacity of a little over 1 million tonnes/year of CO_2 in well CCS2, located about 1 km northeast of CCS1 (well location in Fig. 1a; Fig. 2). As of June 2021, more than 2.5 million tonnes of CO_2 have been injected in CCS2.

The two injection wells (CCS1 and CCS2) are placed about 1 km apart from each other (Fig. 1a) and both wells target the Lower Mt. Simon Sandstone for injection. The injection is into a different high-permeability zone in each well, both relatively near to the top of basement. At CCS1, injection occurred at two perforation depths where most CO_2 was injected in the lowermost perforation interval between 1937–1945 m below sea level (BSL) (Bauer et al., 2016). At CCS2, injection occurred at a slightly shallower depth (46 m shallower than CCS1) in four perforation zones.

In addition, two verification wells, VW1 and VW2, located approx. 300 m north of CCS1 and 800 m northwest of CCS2 injection wells were used to evaluate performance by monitoring in situ pressure, temperature, and pore fluid composition. Whole core and sidewall cores were retrieved from all boreholes along with downhole petrophysical logging to evaluate the hydraulic, mechanical and in situ stress directions and properties of the caprock, reservoir, and basement (Freiburg et al., 2020; Bauer et al., 2016; Morrow et al., 2017). Additionally, Formation MicroImager (FMI) logging was run in all four boreholes to identify sedimentological and structural features, in situ stress direction indicators and dominant fracture sets and their characteristics, which we compare to microseismic event cluster characteristics in Section 4. Core samples of the basement extracted from the four wells were also used for microstructural analysis and dating (Freiburg et al., 2020).

Since the start of injection in 2011, microseismic events have been recorded by borehole geophones and, from June 2013 onwards, by additional USGS and ISGS surface sensors. These surface sensors are only used for focal mechanisms computation and are shown in Fig. 1 in Langet et al. (2020). The geophysical monitoring wells GM1 and GM2, together with PS3 and VW2 are depicted in Fig. 1b. 4293 of the microseismic events detected by these downhole sensors were relocated by Dando et al. (2021) using a modified double difference (DD) relative relocation procedure. The DD-relocations better constrain the events within their respective clusters and show improvements towards clearer, more distinct and tighter spatial event clusters (Fig. 9 in Dando et al., 2021). Most microseismicity occurred during Ph1 (Fig. 2) with a strong decrease in event activity after permanent shut-in and no significant increase of event activity during Ph2. Fine-grained mudstone layers intercepted by the wells at various depths were not correlatable between wells, and were interpreted to represent discontinuous low-permeability lenses occurring within the Lower Mt. Simon Sandstone. These mudstone layers act as baffles that influence fluid-flow and appear to restrict vertical flow, forcing fluid migration to be primarily horizontal (Williams-Stroud et al., 2020). This behavior was observed when comparing the pressure changes in the verification wells, as indicated by the response of pressure gauges at different depths (Greenberg, 2020). The CCS1 injection was conducted in the lowermost part of the Mt. Simon Sandstone reservoir below a lower permeability zone in the middle of the lower Mt. Simon, whereas CCS2 is injecting above this zone. Additionally, Williams-Stroud et al. (2020) attribute the difference in the activity level of the induced seismicity to the difference in the injection interval zones.

Most events are located within the upper 250 m of Precambrian basement with significantly fewer events above the basement and in the Lower Mt. Simon reservoir. For selected clusters, events could be separated in defined sub-clusters using waveform cross-correlation and migration patterns were identified (Goertz-Allmann et al., 2017). Furthermore, Goertz-Allmann et al. (2017) and Goertz-Allmann et al. (2021) analyzed spatial variations of source parameters such as stress drop and Gutenberg's *b*-value for selected event clusters. These variations may indicate differences in the medium or the fault properties and changes in pore pressure. Overall, Goertz-Allmann et al. (2021) concluded that events with lower *b*-values are deeper and further away from the cluster nucleation.

In addition to the updated event catalogue, the 3D seismic reflection cube was reprocessed (survey area corresponds to the extend of the basement map in Fig. 1) showing improved seismic resolution and allowing the identification of faults ranging from 100 to 1200 m in length. Generally, the positions of the faults do not directly correlate with the location of microseismic events (Fig. 1, Williams-Stroud et al., 2020). The faults can be divided into three main sets based on their orientation: (i) N-S striking faults that are more frequent in the east and southeast of the seismic survey; (ii) two WNW-ESE striking faults, to the south of cluster D and (iii) ENE-WSW to E-W across the basement low, between clusters C and G (Fig. 1). Furthermore, a few NE-SW faults have been mapped.

The objective of this paper is to investigate microseismic activity at

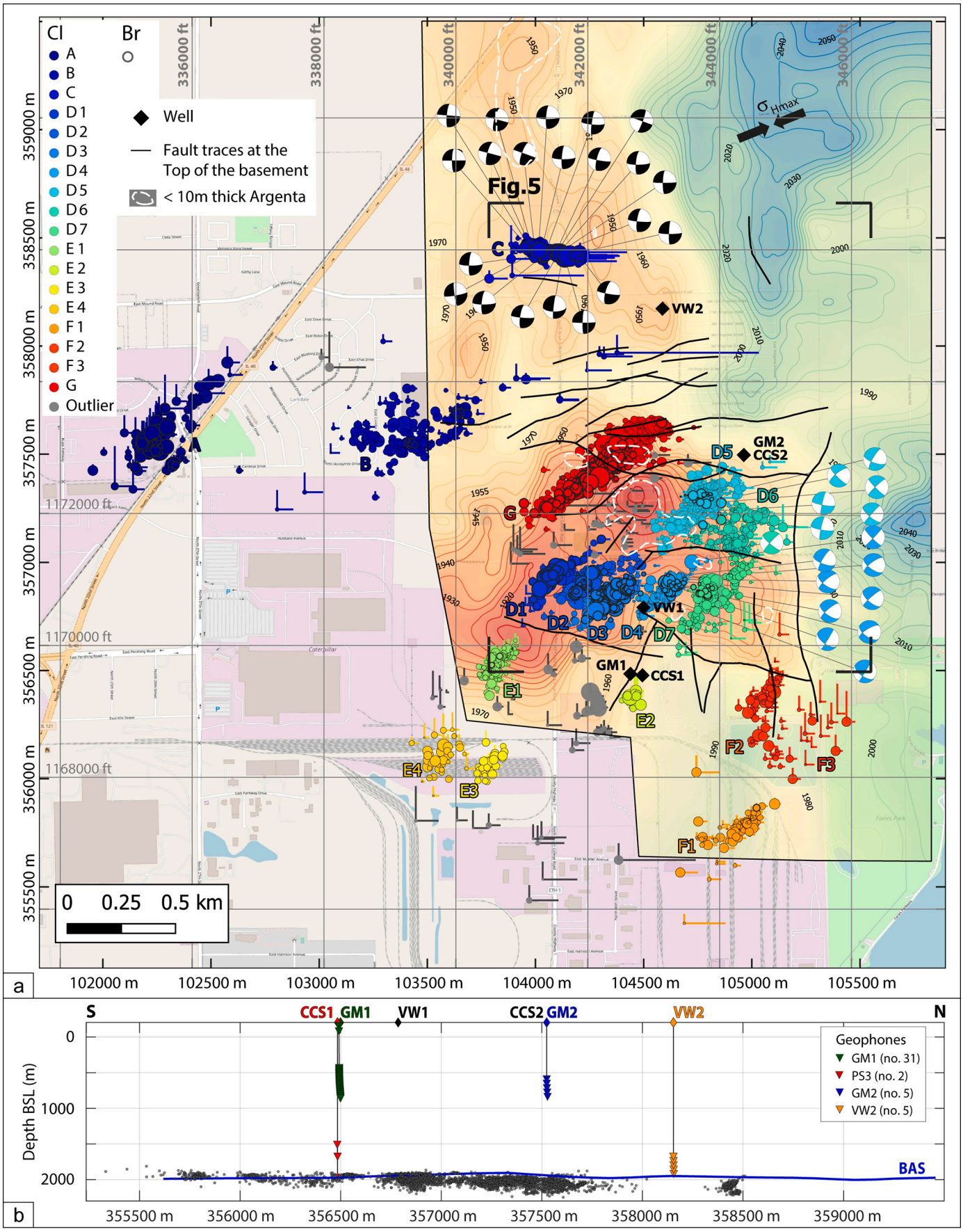

(caption on next page)

Fig. 1. (a) Map view of the seismicity at Decatur showing 18 spatial clusters (Cl) of events labelled A to G. Size of the dots is proportional to event magnitude and the semi-axis at each event represents location uncertainties in East and North directions. Outlier events, i.e. events that do not belong to any of the clusters, are shown as gray dots. The Eastern part of the map shows the topography of the Precambrian basement as interpreted from reprocessed active seismic data (color-coded map and contour lines). Interpreted fault traces at the top of the basement are shown as black lines (Williams-Stroud et al., 2020). White dashed contours indicate small regions where the thickness of the Argenta formation is interpreted to be less than 10 m, or potentially absent (Williams-Stroud et al., 2020). Wells are shown as black diamonds; black arrows (in top right corner) indicate the maximum horizontal stress direction measured at CCS1 and its direction ($\sigma_H = 068°$) measured in all four boreholes with drilling induced tensile fractures and breakout directions from FMI logs and petrophysical sonic anisotropy logs. Focal mechanisms for events in cluster C are from Langet et al. (2020) and for the D clusters from this article, Section 4. (b) N-S cross-section through CCS1 showing the seismic events (gray dots), the top of the basement (BAS) and the microseismic monitoring network. (For interpretation of the references to color in this figure legend, the reader is referred to the web version of this article.)

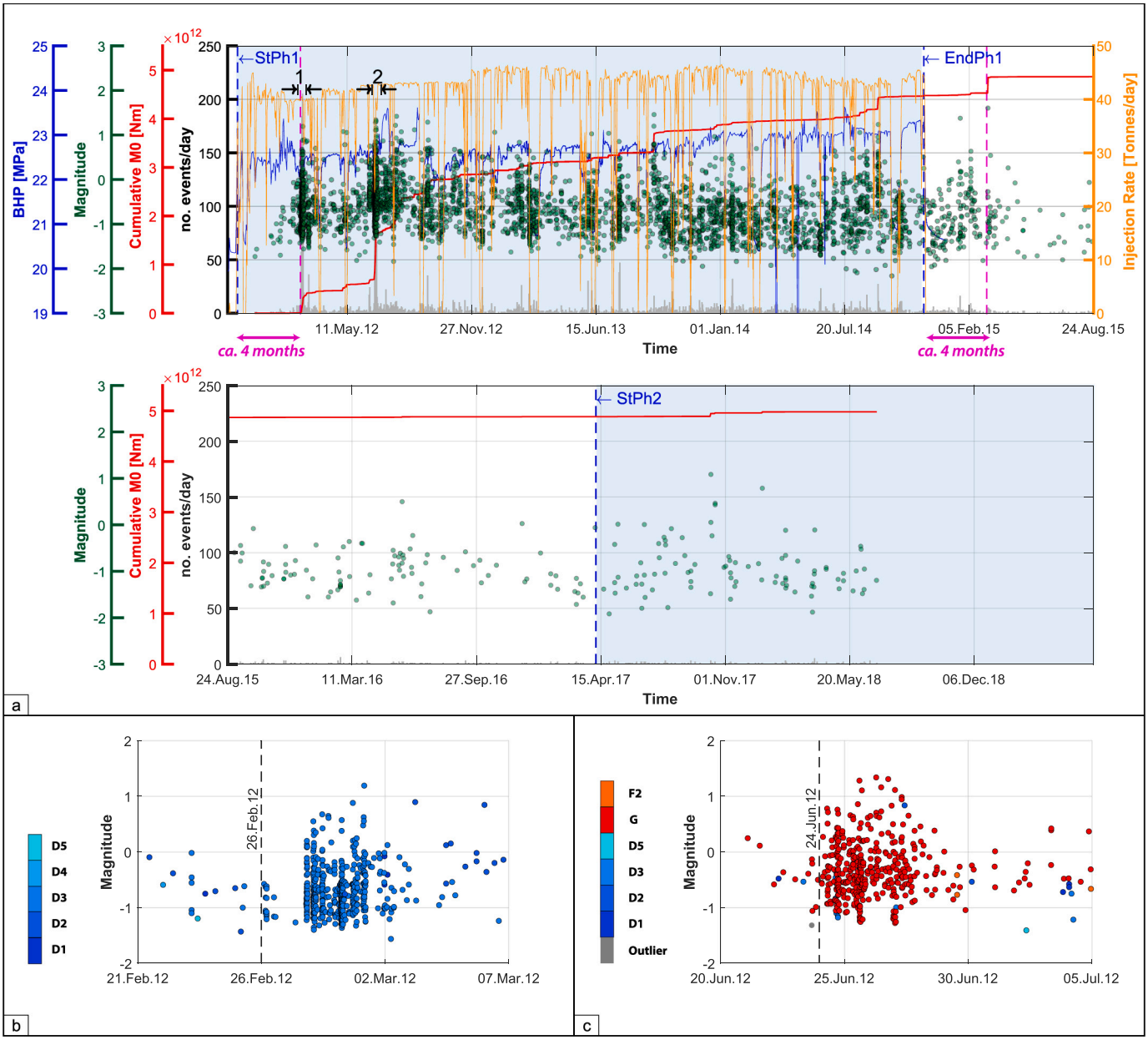

Fig. 2. (a) Magnitude of microseismic events (green dots) as function of time showing abrupt increase of microseismicity (labelled as "bursts" in the following). Note that the timeline in figure (a) is split in two rows for visualization purpose. Bursts are also recognizable by the increase in the cumulative seismic moment (M0, red curve and axis) and in the gray histogram showing the number of events per day. The start (Nov. 17, 2012) and end (Nov. 26, 2014) of the phase 1 injection (Ph1) and the start (April 7, 2017) of the phase 2 injection (Ph2) are shown by dashed vertical blue lines and injection periods are marked by light blue background. The time-lag (ca. 4 months) between the start of the Ph1 injection and the first identified burst is shown by a horizontal magenta arrow, repeated at the end of the Ph1 injection. Injection rates (orange curve) and downhole pressure (blue curve) for the Ph1 injection are also displayed. (b and c) Close-up of two periods of increase in seismicity on February 26, 2012 and June 24, 2012 (indicated by black arrows in (a)) showing different patterns of seismicity: time-discrete in (b) vs. "cloud-like" in (c). Color of the events corresponds to the coloring of clusters, as shown in Fig. 1. (For interpretation of the references to color in this figure legend, the reader is referred to the web version of this article.)

Decatur and show (i) how bursts can help to identify structural weaknesses and complement cluster analysis defining smaller-scale fractures as well as (ii) how clusters and bursts can help to constrain local variations in the stress state. We will demonstrate how the spatial analysis of accurate event locations (employing the DD-catalogue) complements the interpretation of reflection seismic imaging in structural analysis, particularly when investigating subsurface discontinuities below the imaging resolution. Given that seismicity occurs on pre-existing fractures susceptible to slip, we interpret their orientation as extracted from the event locations with respect to the stress field by using slip tendency methods. Furthermore, source parameter analysis (e.g., source mechanisms determined by Langet et al., 2020 and *b*-value analysis by Goertz-Allmann et al., 2021) provides additional information.

The rest of the paper is structured as follows: in Section 2, we provide an overview of the regional geological and reservoir settings at the Decatur site. Particular focus is given to the knowledge of pre-existing fractures at hypocentral depths and to the regional stress state in terms of both orientation and magnitude. In Section 3, we describe the seismicity and how spatial and temporal clusters (or bursts) have been extracted from the updated microseismicity catalogue. In Section 4, we illustrate specific features of selected spatial clusters and bursts in relation to the known stress state. In Section 5, we summarize the major findings and finally, in Section 6 we have concluding remarks.

2. Regional and reservoir geological settings

The Illinois Basin is a large intracratonic basin (approx. 155,000 km^2, Fig. 3) and constitutes a depression slightly elongated in NW-SE direction. It extends through central and southern Illinois, Indiana and Kentucky and is bounded by arches and domes (Yang et al., 2017). Precambrian basement is part of the Eastern Granite-Rhyolite province and a Late Precambrian to Early Cambrian rifting event during breakup of the supercontinent Rodinia is believed to have led to its formation (Freiburg et al., 2020). The basin thickens southwards and is filled with up to approx. 7 km of Paleozoic (Early or Middle Cambrian to Early Permian) sedimentary rocks as consequence of subsidence pulses

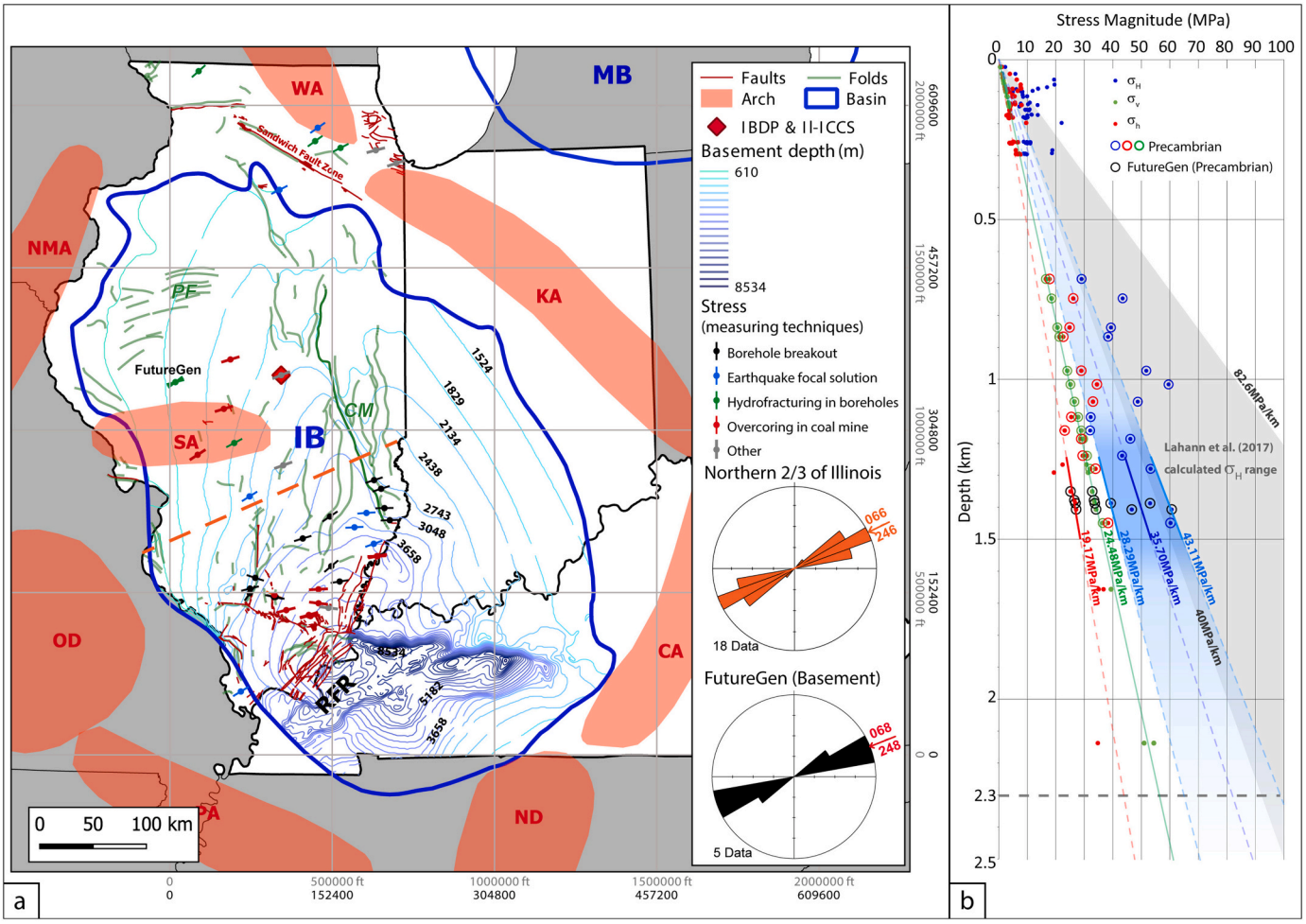

Fig. 3. (a) Map showing the approximate extent of the Illinois Basin (IB, blue outline) spanning the states of central and southern Illinois, Indiana, and Kentucky. Arches and domes, active during various times of the basin's history (Yang et al., 2017) are schematically represented by red shaded areas. The Michigan Basin (MB) is partially shown at the top right. Contour lines represent the basement depth (from 610 to 8534 m) within the IB. Fault traces and fold axes mapped at all depths by a collaborative effort (https://oiink.sitehost.iu.edu/) of Indiana, Purdue, and Illinois Universities as well as the Indiana and Illinois state geological surveys are shown as red and green lines, respectively. The stress orientations are a collection of measurements from various sources. WA = Wisconsin Arch; KA = Kankakee Arch; NMA = Northeastern Missouri Arch; SA = Sangamon Arch; CA = Cincinnati Arch; OD = Ozark Dome; ND = Nashville Dome; PA = Pascola Arch. RFR = Reelfoot Rift. The location of the Decatur site is shown by a red diamond. Rose diagrams in orange and black respectively show the maximum horizontal stress orientation for 2/3 of Illinois (north of the orange dashed line) and for the basement at the FutureGen site. CM = Charleston monocline; PF = Peoria Folds. (b) In situ stress showing the principal stresses. Stress gradients measured at the FutureGen site within the basement are indicated by dashed lines (in blue for σ_H, green for σ_V and red for σ_h). Maximum horizontal stress gradient ranges calculated by Lahann et al. (2017) are indicated for comparison (gray region). Gray dashed line indicates hypocentral depth (TVD from ground level) of microseismic events. (For interpretation of the references to color in this figure legend, the reader is referred to the web version of this article.)

(Kolata and Nelson, 1990). The southern end of the basin is known to display natural seismicity (Tuttle et al., 2002) and to be dominated by Proterozoic rift structures including the Reelfoot Rift-Rough Creek Graben systems that might, to some extent, also control present-day seismicity as suggested by McBride et al. (2007). Another large-scale but low relief structure is the Sandwich Fault zone, located west of the termination of the Kankakee Arch, which separates the Illinois Basin from the Michigan Basin to the northeast (Yang et al., 2017). The remaining part of the Illinois Basin, although not dominated by large-scale structures, did not behave as a rigid block during geological history. This is documented by the presence of mainly N- to NNW-trending folds of the La Salle Anticline and its westernmost frontal culmination, the Charleston monocline, which were active for most of the Paleozoic (McBride, 1997) and located in eastern Illinois. Additional folds include the roughly ENE-striking Peoria Folds, north-northwest of Springfield (Fig. 3). The majority of the folds in the Illinois basin are drag-folds attributed to underlying faults within the basement, such as the La Salle fold which is assumed to be similarly underlain at depth by a reverse intra-basement fault with the overlying Paloezoic strata accommodating its displacement, though when drilled, no evidence of a fault was found (McBride, 1997).

The storage target of both the IBDP and IL-ICCS is the Cambrian Mt. Simon Sandstone, a regionally extensive formation that is divided into Lower, Middle, and Upper Mt. Simon Sandstone (Freiburg et al., 2014). The Mt. Simon Sandstone reaches a maximum thickness of approx. 790 m in northeastern and east-central Illinois (Leetaru and McBride, 2009). The Lower Mt. Simon Sandstone has been further divided into two units (A and B) based on major depositional facies (Freiburg et al., 2014). The best reservoir quality rocks are in the Lower Mt. Simon Sandstone (average porosity of 22% and 28% as well as permeability of 200 mD and 250 mD at CCS1 and CCS2, respectively), while the Middle Mt. Simon Sandstone has poor reservoir properties, mainly due to diagenetic quartz cementation (Leetaru and Freiburg, 2014). The Mt. Simon Sandstone is overlain by the Eau Claire Formation, which is the primary seal (approx. 150 m thick). The Argenta formation, formerly known as pre-Mt. Simon, underlies the Mt. Simon and overlies unconformably the igneous Precambrian Basement. This unconformity is also known as the sub-Sauk or Great Unconformity, and corresponds to an approx. 900 Ma hiatus (Leetaru and Freiburg, 2014). The Argenta formation is characterized by significantly lower porosity and permeability compared to the reservoir (Freiburg et al., 2014). The Precambrian basement is compositionally heterogeneous and structurally complex, mainly made of rhyolite, although gabbro, granite, and volcaniclastic breccia have been penetrated by the CCS1, CCS2 and VW1 and VW2 wells (Freiburg et al., 2020). Furthermore, an approx. 5-m thick trachyte dyke intruding the volcanoclastic breccia has been observed at VW1 (Freiburg et al., 2020).

Within the area covered by the reprocessed active seismic data, the basement at the Decatur site is located between 1903 and 2054 m BSL (Fig. 1) and its topography is characterized by a distinct variation in elevation: topographic highs occur in the western part of the survey area and lows in the eastern part. This elevation change east of VW2 occurs along a NNW-SSE trend. The high relief area to the west is divided by an irregular ENE-WSW trending basement low ca. 800 m north of CCS1. Freiburg et al. (2020) interpreted this topographic low acting as lithological compartmentalization boundary for the basement on the basis of wells located north and south of the topographic low that penetrate the uppermost basement rocks.

The Argenta formation shows thicknesses of up to 87 m. Close to the basement high north of VW1, the thickness is less than 10 m and the Argenta might be absent (Fig. 1). Freiburg et al. (2014) described the basal 30 cm of the Argenta as completely bleached with traces of vertical fractures showing slight diagenetic alteration, which suggests past fluid migration. Sidewall cores and FMI logs from VW1 and VW2 indicate that the Precambrian basement is highly fractured. Fractures are commonly mineralized with calcite cement and in places, likewise show diagenetic alteration, which suggests past fluid migration (Freiburg et al., 2014; Will et al., 2014).

To ensure CCS storage feasibility, 2D seismic profiles were initially acquired. In 2010, 3D seismic surveys were conducted targeting the area that would likely be affected by the CO_2 plume. In 2011, this survey was extended to provide coverage to the north of the site and later, in 2015, the entire survey was repeated to monitor reservoir response to the CO_2 plume (Bauer et al., 2019). Challenges in the acquisition and processing of the 3D seismic data were primarily the high levels of anthropogenic noise, since the site is located within an industrial area, nevertheless suitable results for structural interpretation were obtained (Bauer et al., 2019). By integrating petrographic analysis, geophysical logs, and drill cores from the four wells with the first-processed three-dimensional seismic reflection volume, Freiburg et al. (2020) investigated the basement. They analyzed 16 m thick depth slices (between 1965 m and 2080 m BSL) of a 3D semblance attribute cube and interpreted a series of ENE-WSW and NNW-SSE striking discontinuities in the basement (Fig. 8 in Freiburg et al., 2020).

Although faults were not visible in the first processed volume, reprocessing provided a large improvement of resolution that allowed to identify for the first time faults between 100 m and 1200 m long extending from the cover sequences into the basement (Williams-Stroud et al., 2020). A comparison between the original processed and reprocessed seismic cross-section is shown in Fig. 4 in (Williams-Stroud et al., 2020). Their fault traces at the top of the basement are shown in Fig. 1. Furthermore, a new porosity inversion calibrated with petrophysical properties measured at the wells greatly reduced the uncertainty of the horizon picks and more clearly illuminated the contacts between the Argenta formation and the underlying igneous basement. Recent work on the pressure response at CCS1, VW1 and VW2 due to the injection at the CCS2 allowed us to interpret reservoir heterogeneities that influence vertical and horizontal flow.

2.1. *In situ stress, regional and at the site*

We collected stress state information from multiple sources for Illinois and the Illinois Basin (e.g., Bauer et al., 2016; Lahann et al., 2017; Cornet, 2014). The stress field orientation with the maximum horizontal stress (σ_H) azimuth between 060° and 075–080° is consistent with the eastern part of the North American plate, although local variations close to major structures have been observed (Bauer et al., 2016; Lahann et al., 2017). There are 6 sites with in situ stress measurements within about 64 to 113 km (40 to 70 miles) of the IBDP site that used hydraulic fracturing, overcoring, or strain relaxation (Bauer et al., 2016, Fig. 3a). The average maximum stress direction for the northern 2/3 of Illinois is 066° (rose diagram in Fig. 3a).

Stress gradients were primarily calculated from hydraulic fracture records or extended leak-off tests as well as summation of strata density data for vertical gradients (Lahann et al., 2017). The σ_V gradient is estimated to 24.9 MPa/km and 27.1 MPa/km, above and below 2134 m depth BGL (below ground level, representing an approximation of the basement depth across the basin; Lahann et al., 2017). The σ_h gradient was calculated to range between 24.1 MPa/km and 27.3 MPa/km. The σ_H estimate based on a critically stressed fault model yielded values between 40.0 MPa/km and 82.6 MPa/km (Lahann et al., 2017, gray range in Fig. 3b).

Different measuring techniques of in situ stress show that the stress regime at Decatur is strike-slip ($\sigma_H > \sigma_V > \sigma_h$), for most of the lithologies with higher shear strength, including the basement. Certain depth sections of boreholes CCS1, CCS2, VW1 and VW2 show failure stress indicators related to the in situ stress interpreted from Formation MicroImager (FMI) logs. Numerous tensile opening and tensile shear fractures occur in the Argenta and the Upper and Middle Mt. Simon formations and some in the Precambrian. All are produced during drilling in reaction to the in situ stresses. These drilling induced tensile fractures also indicate a strike-slip or nearly strike-slip stress regime.

Breakouts are common within the Argenta interval in CCS2 and the Lower Mt. Simon in VW2. Both breakouts and tensile fractures show an average azimuth of 068° for the maximum horizontal principal stress (Bauer et al., 2016), with averages between 063° and 071° for the single dataset and 071° for 6 tensile induced fractures in the basement at VW1 (Fig. 5d). Five measurements in the Precambrian basement taken at the FutureGen site, 97 km west of IBDP, show the average maximum stress direction at 068° and a range of 062° to 077°, which is consistent with what observed at Decatur. Furthermore, a range of stress magnitude gradients have been measured at FutureGen in the basement, yielding values between 28.29 MPa/km and 43.11 MPa/km calculated for the maximum principal σ_H and measured between 18.62 to 19.38 MPa/km with an average of 19.17 MPa/km for the σ_h (Cornet, 2014, Fig. 3b). Given the large similarity of reservoir and basement rocks at the two sites, the proximity to the sites and the same σ_H azimuth, we believed that these measurements are representative of the stress state at the Decatur site. The magnitudes for the maximum principal σ_H calculated by Lahann et al. (2017) (using a coefficient of fault frictions as high as 1.0) are about twice as high as what was otherwise calculated using measurements in the Illinois Basin and in the basement at FutureGen, and in particular when comparing with measurements relatively close to the Decatur site (Fig. 3b).

3. Microseismicity at the Decatur site

Microseismic events are distributed in distinct spatial clusters over an area of approximately 9 km^2 around the injection wells (Fig. 1). The maximum measured pore pressure increase at 300 m from CCS1 during Ph1 (1.2 MPa) resulted in a pore pressure that was far below the formation fracture pressure (Bauer et al., 2016, 31.6–34.2 MPa at the depth of injection). There is no clear relation between injected volumes and seismicity (e.g., Goertz-Allmann et al., 2017) and no observed relation between distance of recorded events to injection points and time of occurrence. This suggests that the events are most likely induced by small stress field changes, pore-pressure increase or by Coulomb stress transfer, causing reactivation of pre-existing fractures. Such pre-existing structures were interpreted visually based on the semi-linearity in plan-view of a part of the seismic clouds and observed to align with linear texture in a curvature map obtained from the originally-processed active seismic data (e.g., Will et al., 2014). Goertz-Allmann et al. (2017) analyzed event migration patterns along selected clusters and interpreted basement-reservoir connected faults or fractures.

Dando et al. (2021) reprocessed the waveform data and relocated 4293 events, constituting a new catalogue (DD-catalogue) covering the period between December 15, 2011 and July 2, 2018. Of these events, 3847 occur during Ph1 injection at CCS1, 325 during the inter-injection phase and 121 since the beginning of the Ph2 injection at the CCS2 well. Although the injection rates average 1.7 times higher within CCS2, based on cumulative CO_2 injected by the end of 2020, this rate increase is not accompanied by a corresponding rise in microseismicity. Various short periods of shut-in (temporary hold in injection) occurred during Ph1 and are recognizable in injection rate and downhole pressure (orange and blue curves in Fig. 2, respectively) and these are likewise not accompanied by a decrease or increase in event rates.

The DD-catalogue provided event locations, which are more tightly clustered spatially revealing more precise linearized features. Furthermore, particularly during Ph1, seismicity is characterized by sudden increases in the event rate for short time periods. Such increases may be defined as “seismicity bursts”, and are sometimes also referred to as “temporal event clusters” as opposed to “spatial clusters” (e.g., Vidale and Shearer, 2006). Bursts have been recognized in other geological settings, particularly in relation to pre-eruptive magmatic processes, but also associated to natural and induced seismicity, e.g., during seismic swarms in Iceland (Duboeuf et al., 2021), and at the Weyburn CCS site, Saskatchewan, Canada (Verdon, 2016). Such bursts have also been observed to expand spatially over time, probably caused by pore pressure fluctuations (Vidale and Shearer, 2006).

Our motivation for analyzing seismicity bursts is that we see an increasing potential to attribute dynamic stress field changes to reservoir-scale features based on the interpretation of bursts. Events that occur relatively close in space and time are most likely triggered by a similar physical mechanism that reveals the fault/fracture characteristics and strike and allows to infer pore pressure and stress changes. These events may further delineate discrete fractures and smaller-scale discontinuities within the larger spatial clusters. Bursts can highlight a spatio-temporal evolution and other patterns that may allow a better understanding of stress propagation, gradually revealing the causative plane. Information on the causative fault planes is usually obtained from focal mechanisms and additional geological data; however, to achieve reliable and precise focal planes, the sensor network needs to provide sufficient azimuthal coverage with clear onset observations. At Decatur for example, focal mechanisms could therefore only be determined within two specific regions. In the northernmost clusters C, 23 focal mechanisms were computed by Langet et al. (2020) using a combination of both downhole and surface data. Following the same methodology, 16 additional mechanisms are computed for this study for region D and presented in Section 4.

In the following section, we introduce the selection process of both clusters and bursts and how they can complement other types of analysis and data in defining geological structures.

3.1. Criteria for cluster selection

Clustering of seismic events at Decatur occurred during Ph1 and clusters were interpreted to represent discontinuities on the basis of their semi-linearity in plan-view (e.g., Will et al., 2014), but with an increase in number of seismic events, some clusters progressively revealed a different orientation from what was originally hypothesized.

In this study, we manually define 18 distinct spatial clusters from the (Dando et al., 2021) catalogue (Fig. 1). For computational reasons, the events were split in seven regions (named A to G) during the relocation procedure, based on their geographical location. It was shown by Dando et al. (2021) that these regions feature different degrees of location uncertainties due to the uneven station distribution (Fig. 1). In the following, we refer to the clusters by these regions and, in the case of more than one cluster occurring in the same region, use an additional number. Some outliers (approx. 6%) are not assigned to any cluster as they constitute sparse events in-between clearly recognized clusters (marked as gray dots in Fig. 1).

From these 18 clusters, we extract a series of statistical and geometrical parameters, which are listed in Table 1 and described in the following section. These parameters aim to characterize the clusters in terms of shape and location. For each cluster, the principal axes of the best-fitted ellipsoid, computed from the 3D locations of the event cloud, provide information on the seismicity pattern and trend within each cluster. For instance, the shape of the ellipsoid defined by the ratio of its axes can help to recognize if the seismicity delineates a near-prolate ellipsoid (cigar-shaped, one axis is significantly longer than the other two), a near-oblate ellipsoid (disk-shaped, two axes are significantly longer than the third) or a near-spheroid ellipsoid (all axes are of relatively similar length). A measure of these shapes can be defined by the planarity and linearity coefficients, both ranging from 0 to 1. In the following, we define the planarity as $Pl = 1 - 2\lambda_3/(\lambda_1 + \lambda_2)$ and the linearity as $L = 1 - (\lambda_2 + \lambda_3)/2\lambda_1$, where $\lambda_1 \leq \lambda_2 \leq \lambda_3$ are the eigenvalues representing the length of the ellipsoid semi-axes. These coefficients are also used to define the type of structure as planar ($Pl > L$), linear ($L > Pl$) or cloud (either Pl or $L < 0.7$, an arbitrary value chosen during visual inspection). The minor axis of the ellipsoid is normal to the fault plane. Hence, the dip angle coincides with the angle between minor and vertical axis. The fault strike is derived from the dip direction, which is the angle between the minor axis projected at the surface and geographic North. The convention used here is based on the right-hand-

Table 1
Summary of the 18 clusters and extracted parameters. Cl = cluster name; C.E. = centroid Easting [m]; C.N. = centroid Northing [m]; C.D. = centroid depth [m, BSL]; Pl = planarity; Lin = linearity; RO = no. of removed outliers; No. = number of events; Den. = 3D density [No./m^3]; St = strike; M0 = net seismic moment [Nm]. * = not well-constrained. ** = not constrained. Bold rows represent clusters that we focus on in this study.

Cl.	C.E.	C.N.	C.D.	Type	Pl	L	RO	No.	Den.	St (°)	Dip (°)	M0
A	102,272	357,572	2129	Plane	0.80	0.70	11	123	4.5e−6	48	35	0.4524e12
B	103,491	357,621	2037	Line	0.80	0.86	14	271	4.9e−6	254	52*	0.1066 e12
C	**104,066**	**358,439**	**2102**	**Plane**	**0.94**	**0.77**	**8**	**211**	**3.42e−5**	**282**	**85**	**0.6337e12**
D1	**104,072**	**356,915**	**1993**	**Line**	**0.90**	**0.90**	**5**	**91**	**1.72e−5**	**229**	**73***	**0.2530e12**
D2	**104,230**	**356,913**	**1982**	**Plane**	**0.82**	**0.80**	**18**	**197**	**5.11e−5**	**238**	**90**	**0.2440 e12**
D3	**104,343**	**356,831**	**1979**	**Plane**	**0.77**	**0.70**	**57**	**940**	**3.3e−4**	**235**	**80**	**0.5527e12**
D4	**104,611**	**356,880**	**1963**	**Cloud**	**0.83**	**0.69**	**13**	**148**	**3.62e−5**	**55****	**64****	**0.0528e12**
D5	**104,770**	**357,280**	**2053**	**Line**	**0.74**	**0.79**	**33**	**407**	**4.3e−5**	**48**	**63***	**0.2440e12**
D6	**104,930**	**357,121**	**2024**	**Cloud**	**0.86**	**0.58**	**11**	**163**	**1.37e−5**	**80****	**4****	**0.0240e12**
D7	**104,830**	**356,848**	**2061**	**Plane**	**0.76**	**0.75**	**6**	**170**	**7.9e−6**	**233**	**49**	**0.0855e12**
E1	103,826	356,528	1950	Line	0.71	0.78	6	115	3.97e−5	78*	16*	0.0062 e12
E2	104,448	356,370	1996	Cloud	0.78	0.57	–	15	1.42e−5	220*	57*	0.0190 e12
E3	103,775	356,051	1949	Plane	0.79	0.78	3	38	3.59e−5	36	41	0.0120 e12
E4	103,556	356,103	1973	Cloud	0.74	0.60	4	40	5.3e−6	339*	34*	0.0138 e12
F1	104,945	355,776	1945	Line	0.82	0.88	4	98	1.37e−6	45	24*	0.0199 e12
F2	105,067	356,381	2038	Line	0.78	0.82	4	52	3.6e−6	27	57*	0.0139 e12
F3	105,203	356,171	1983	Plane	0.96	0.82	1	29	2.6e−6	211	23	0.0024 e12
G	**104,320**	**357,452**	**2025**	**Line**	**0.92**	**0.93**	**60**	**843**	**5.25e−5**	**234**	**66***	**2.0858e12**

rule (RHR). Furthermore, the strike and dip angles of the best fitting plane are only representative of the underlying structure for near-prolate and near-oblate ellipsoids. However, the strike is only well constrained if the major axis of the near-prolate ellipsoid is sub-horizontal, while the dip might be affected by uncertainty.

It is worth noting that the shape of the ellipsoid may be quite sensitive to potential outliers, especially if the number of events is small. Thus, we remove all events with locations at distance to the ellipsoid centroid larger than two standard deviations. Finally, we define the event density within each ellipsoid to be the number of events in the ellipsoid per unit volume (No./m^3). To that end, we considered the volume of the 95% confidence ellipsoid.

3.2. Criteria for burst selection

Bursts can be identified manually or automatically. A manual selection of bursts highlighted that the duration of each burst and the number of events contributing to it is highly variable; therefore, defining

Table 2
Summary of the 35 bursts. N. = burst number; No. = number of events; Cl. = cluster in which the events occur; C.E. = centroid Easting [m]; C.N. = centroid Northing [m]; C.D. = centroid Depth [m, BSL]; Dist. = distance between centroid and injection point [m]; Pl = planarity; L = linearity; St. = strike.

N.	No.	Cl.	C.E.	C.N.	C.D.	Dist.	Type	Pl	L	St. (°)	Dip (°)
Br1	13	**D3**	10,403	356,819	2035	398.9	Plane	0.78	0.71	231	85
Br2	55	**D3**	104,070	356,825	2013	384.3	Plane	0.87	0.79	233	55
Br3	96	**D3**	104,076	356,823	1981	374.2	Cloud	0.81	0.50	238**	60**
Br4	41	**D3**	104,076	356,827	2008	383.1	Line	0.71	0.74	213	66*
Br5	16	**D3**	104,083	356,836	1968	381.7	Cloud	0.85	0.66	248**	78**
Br6	142	**D3**-D2	104,061	356,815	1959	370.9	Plane	0.85	0.77	236	71
Br7	53	**D3**	104,123	356,861	1990	395.9	Plane	0.79	0.78	67	71
Br8	45	**D3**	104,132	356,869	1997	402.9	Cloud	0.68	0.61	75**	78**
Br9	29	**D2**-D1	103,937	356,878	1960	488.8	Cloud	0.79	0.60	313**	8**
Br10	17	**G**-D2	103,845	357,284	1981	887	Plane	0.99	0.99	71	31
Br11	18	**G**	103,977	357,396	2019	950.3	Plane	0.91	0.80	247	85
Br12	65	**G**-D3	104,027	357,422	2008	962.3	Line	0.84	0.85	238	81**
Br13	97	**G**-D3	104,021	357,417	1993	957.5	Plane	0.94	0.94	245	45
Br14	18	**G**	103,997	357,397	2008	944.9	Plane	0.92	0.92	238	60
Br15	32	**G**-D3	104,045	357,448	2036	987.4	Plane	0.86	0.80	244	66
Br16	21	**G**-D3	104,053	357,458	2025	994.1	Plane	0.90	0.88	62	76
Br17	20	**G**	104,035	357,421	2012	960	Plane	0.87	0.87	250	84
Br18	34	**D1**-G	103,792	356,929	2013	626.2	Plane	0.95	0.91	224	41
Br19	11	**D5**-G	104,521	357,271	2022	848	Plane	0.94	0.91	240	12
Br20	18	**G**	104,103	357,536	2026	1064.5	Plane	0.95	0.95	260	38
Br21	21	**D3**-E1	104,110	356,883	2027	427.8	Plane	0.83	0.76	234	71
Br22	15	**D3**	104,070	356,862	1975	411.3	Plane	0.91	0.90	54	44
Br23	25	**D3**	104,040	356,839	2026	412.3	Cloud	0.80	0.56	51**	87**
Br24	22	**D3**	104,069	356,869	1951	416.5	Cloud	0.73	0.65	238**	56**
Br25	23	**D3-D7**-E1	104,039	356,849	1961	411.3	Plane-Plane	0.95–0.90	0.93–0.70	70–316	68–40
Br26	21	**D3**	104,000	356,765	1952	360.5	Cloud	0.75	0.44	240**	84**
Br27	36	**D3**	104,037	356,794	1953	363.6	Cloud	0.81	0.66	233**	63**
Br28	20	**A**-F1	101,951	357,564	2133	2524.5	Plane	0.96	0.92	21	19
Br29	11	**A**-D5	101,982	357,549	2182	2494.5	Cloud	0.40	0.46	114**	63**
Br30	12	**B**	103,150	357,549	1963	1512.4	Plane	0.97	0.84	66	27
Br31	43	**D4**	104,363	356,890	1970	432.7	Cloud	0.84	0.47	76**	51**
Br32	16	**D5**	104,497	357,309	2012	874.6	Plane	0.98	0.96	268	84
Br33	18	**C**	103,746	358,434	2056	2013	Cloud	0.88	0.65	292**	83**
Br34	28	**C**	103,838	358,426	2102	1989	Plane	0.94	0.83	101	81
Br35	16	**C-B**	103,904	358,413	2101	1964	Plane-Plane	0.87–0.97	0.76–0.91	97–102	58–82

an exact criterion to automatically select bursts can be challenging. The method we employ is based only on the event origin times and thus, differing from other existing studies which also include a spatial constraint (e.g., Vidale and Shearer, 2006). Therefore, a burst may include events from more than one cluster (Table 2). This choice is dictated by our interest in determining if out-of-cluster events may highlight a migration pattern from one cluster to the next or if seismicity bursts occurring simultaneously at different locations may indicate of similar pressure front conditions.

The two largest increases in seismicity rate on February 26 and June 24, 2012 (black arrows in Fig. 2a, close-up view in Fig. 2b) show a different pattern. The first of these two periods of increased seismicity is characterized by well-defined temporally discrete bursts, which renders the extraction of bursts simpler and unequivocal. The second time period shows a more "cloud-like" pattern with less clearly defined bursts.

Considering that bursts consist of a number of events occurring within a relatively short period of time, we scan through the event timeline to identify consecutive events that occur within a time range shorter than a predefined threshold value f, which is a measure of frequency of occurrence. The schematic diagram in the inset in Fig. 4a shows an example for a threshold of $f = 1$. Events i are represented as black dots occurring at different times t_i (t_1, t_2, …) and event intervals are defined as $\Delta t_i = t_{i+m} - t_i$, where m is the number of event intervals (e.g., two events correspond to one event interval, $m = 1$, three events, $m = 2$, etc.). For $m = 1$ the events will represent a burst if the event interval $\Delta t_i \leq 1/f$ (see blue and green check marks). This procedure was repeated for an increasing number of event intervals m, which can be defined as $m =$ No. -1, where No. is the number of events. In Fig. 4, the color plot shows $log_{10}(m/\Delta t_i)$ for all the events i as a function of a mean interval time $(t_{i+m} + t_i)/2$ for m between 10 and 370 (10 and 370 were considered as end members for the number of event intervals in the manually selected bursts).

Bursts are represented in Fig. 4a in red ($log_{10}(m/\Delta t_i) \geq 2$). White gaps correspond to time periods where large inter-event times are observed. Fig. 4 illustrates that bursts mainly occur during Ph1 (Fig. 4a) with only

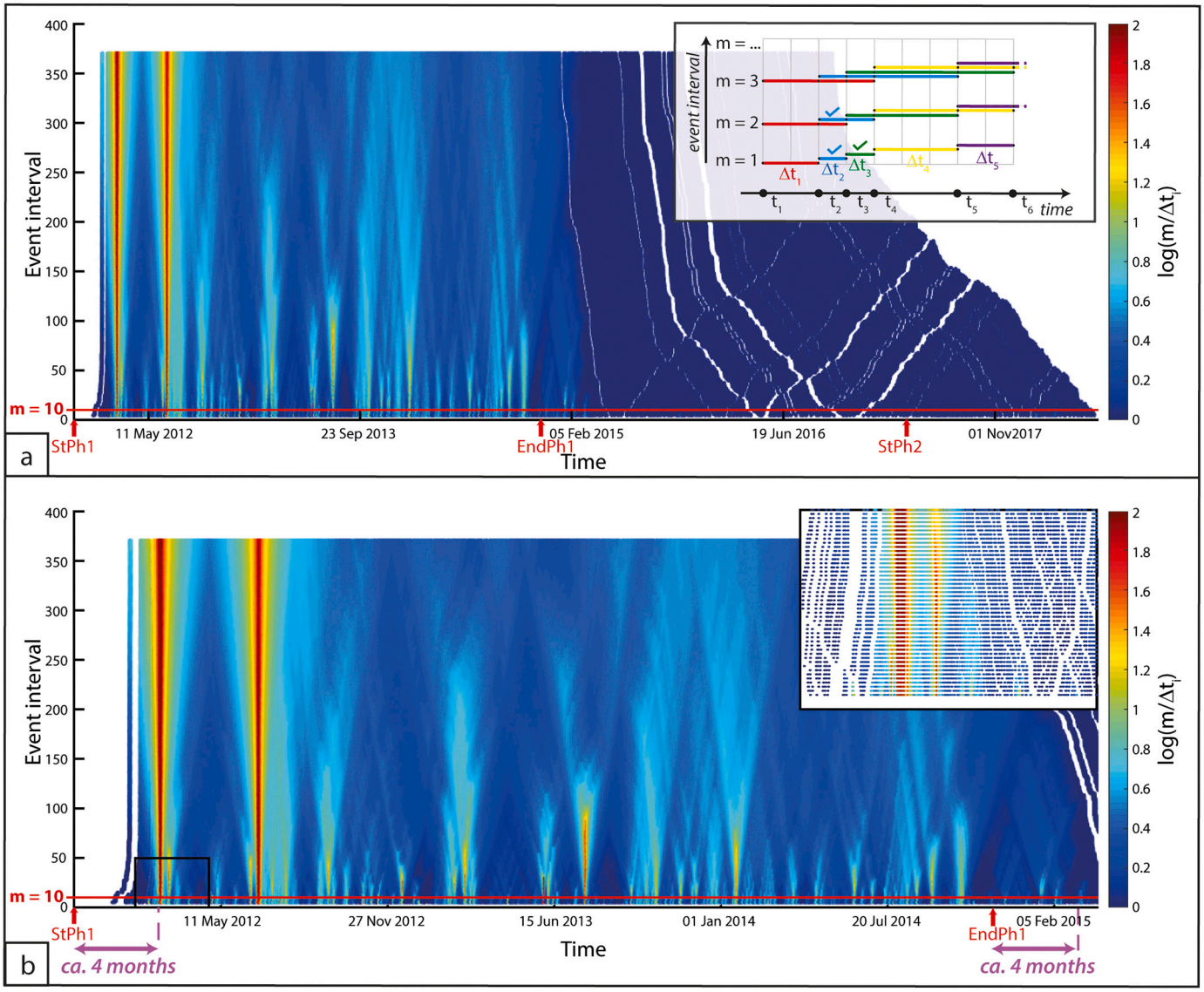

Fig. 4. Average event frequency over time vs. event interval time for (a) the entire injection period and (b) the period in which bursts have been identified. Red arrows indicate the start of Ph1 (StPh1), the end of Ph1 (EndPh1) and the start of Ph2 (StPh2). The horizontal red line corresponds to the event interval $m = 10$. Inset in (a) is a schematic representation of the method used to extract bursts from the catalogue. Events are represented by black dots and intervals by colored bars. Intervals representing bursts are marked with check symbols. Inset in (b) is a close-up of the black box. (For interpretation of the references to color in this figure legend, the reader is referred to the web version of this article.)

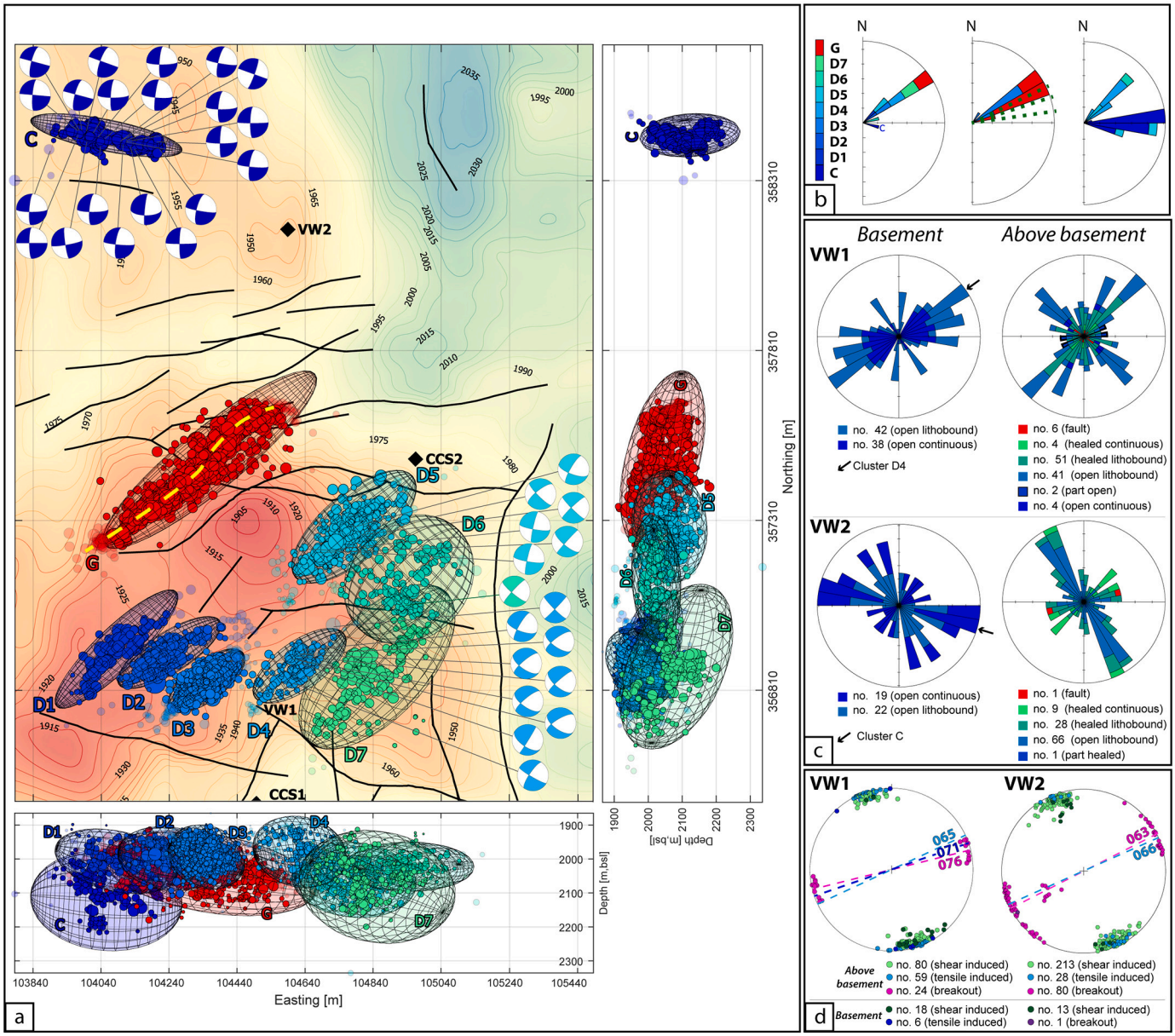

Fig. 5. (a) Combined map-view and vertical east-depth and north-depth panels showing clusters C, D1–D7, G and their event ellipsoids. Color scheme corresponds to Fig. 1 and the size of the dots is proportional to event magnitude. The yellow dashed line shows the plan-view shape of cluster G. Wells are shown by black diamonds. Selected focal mechanisms are reported for cluster C (Langet et al., 2020), D4, D5, and D6. (b) Rose diagram showing the extracted strike of (left) clusters, (center) bursts and (right) interpreted from the focal mechanisms. (c) Rose diagrams of the strike of fractures intercepted by VW1 (top) and VW2 (bottom) both at basement depths (left) and above (right) the basement. The strikes of clusters C and D4, which are the closest clusters to the two verification wells, are indicated by black arrows on the respective rose diagrams. (d) Equal-area lower-hemisphere stereonet plots showing poles to induced fractures and breakouts as interpreted at VW1 and VW2, above and below the basement. Light blue and the magenta dashed lines (and labels) indicate the mean azimuth for the horizontal stress from the plotted tensile induced fractures and breakouts, respectively. Blue dashed line (and label) indicates the mean azimuth for the horizontal stress from tensile induced fractures in the basement. (For interpretation of the references to color in this figure legend, the reader is referred to the web version of this article.)

one burst occurring after the end of this injection phase, containing only a few events. Note that large inter-event times are only observed after Ph1. Fig. 4b shows the time range in which bursts have been recognized.

For a value of $m = 10$, the automatically and manually selected bursts were comparable in terms of total number, number of events, and duration. An overview of manual, automatic, and final selection of bursts is reported in Table S1 in the supplementary material. During the automatic selection process, a larger number of bursts could be identified compared to the manual analysis, in part due to the subdivision of manually recognized bursts.

Only in one case, two manually identified separate bursts were not correctly split by the automatic process, probably because they were consecutive.

Therefore, the final selection of 35 bursts analyzed in Section 4 is extracted from both manual and automatic processing (Fig. 1, Figs. S1 and S2 in the supplementary material). Similar to the cluster analysis, strike, dip, and planarity were extracted for the bursts by defining both the event ellipsoid and burst centroid (Table 2).

4. Spatial and temporal patterns in event clusters

4.1. Spatial patterns

Cluster distribution at Decatur is irregular with 8 of 18 clusters

(Fig. 5a) occurring in an approximately 1 km^2 area north of VW1. To the north and west of this region, clusters are separated by larger distances (Fig. 1). To the west, clusters A and B are composed of sparser events, with intermittent denser clustering. The location uncertainty of most relocated events is relatively low (Fig. 1 and Dando et al., 2021). An apparent overall plan-view linearity can be inferred for cluster A but it also has the largest event location uncertainty. For cluster B, a similar overall plan-view linearity is poorly defined, due to the scattered spatial distribution of the events. To the north, cluster C features an event density that is one order of magnitude higher compared to clusters A and B (Table 1). In addition, events exhibit a clear plan-view linearity in E-W direction. The highest event density occurs in cluster D3 with 997 events (equivalent to a density of 330,000 events/km^3), followed by cluster G with 903 events (equivalent to a density of 52,500 events/km^3) (Table 1). Cluster G spans the largest area (approximately 780 m × 250 m) and has an overall orientation similar to clusters D1–D5, and D7 (Fig. 5a and b).

Clusters with higher numbers of events and with higher event density may also provide more reliable information on underlying structures and processes. Furthermore, a statistical analysis of these clusters with spatial *b*-value variations also led to more stable and reliable results for these clusters (Goertz-Allmann et al., 2021). Spatial *b*-value variations as estimated by Goertz-Allmann et al. (2021) are presented for clusters G, D3, D5, and C in Fig. 6. For each event within these clusters, the *b*-value was calculated using a fixed number of neighboring events and color-coded according to the calculated *b*-value. The magnitude of completeness was also estimated separately for each computation. We adjusted the input parameters depending on the individual cluster extent and overall number of events within a cluster. We used the closest 50 events for cluster C, 150 events for cluster D5 and G, and 300 events for cluster D3.

In the following section, we will focus on a more detailed description of clusters D1–D7, C, and G, which (i) occur in the area for which 3D active-source seismic data have been reprocessed, and (ii) feature the highest numbers of events and high event density (Fig. 5). Moreover, the clusters are situated relatively close to the injection and/or verification wells allowing for integration of further information.

4.1.1. *Clusters D1 to D7*

Clusters D1 to D4 and D7 are altogether located in a E-W elongated region approx. between 356,500 m and 357,000 m North. Each of the clusters shows a NE-SW elongation in map-view, as demonstrated by the strike extracted from their event ellipsoids (≤11° strike difference, Table 1 and Fig. 5b). These clusters potentially delineate an en-echelon arrangement of faults which is geometrically described by their arrangement (e.g., separation or distance between faults, measured orthogonally to strike and overlapping length, measured along-strike) in plan-view. Clusters D1–D3 overlap, and are separated by about 100 m each (Fig. 5). D4 and D7 are both more separated from the previous clusters, and the overlap of D3 and D4 is smaller. Note that both D4 and D6 have been defined as clouds (Table 1), however, the strike of D4 is nevertheless consistent with the other clusters, which is not the case for cluster D6, which moreover is poorly constrained. In addition, the plane extracted from cluster D6 is the only sub-horizontal plane in this region

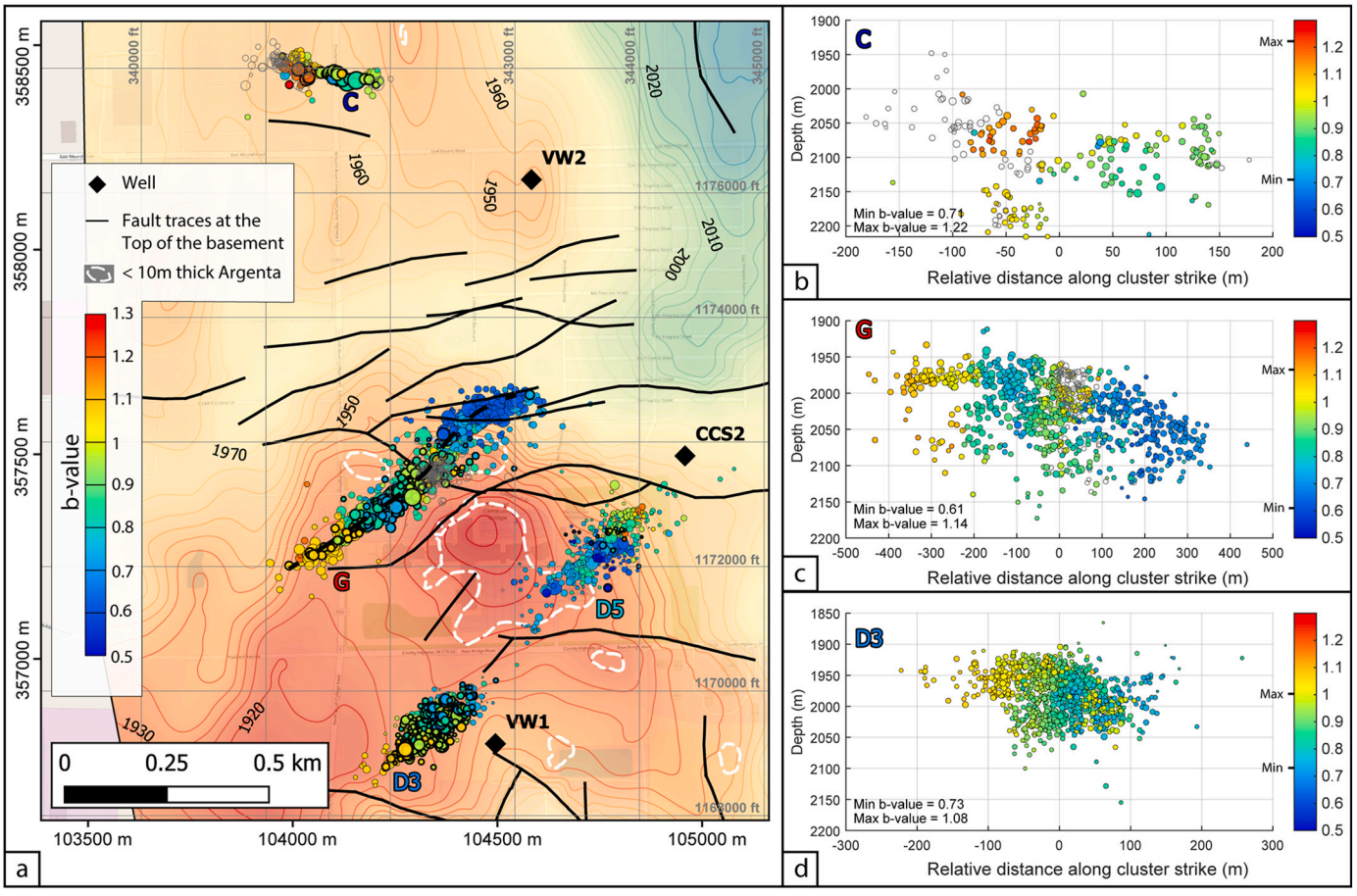

Fig. 6. (a) Map view showing the spatial variation of the *b*-value calculated for clusters D3, D5, C and G as colored dots. Events marked by a thicker outline are part of bursts. The shape of cluster G is shown as black dashed line. Top of the basement with contour lines and faults (black lines) is also shown. White dashed contours indicate small regions where the thickness of the Argenta formation is interpreted to be less than 10 m, or potentially absent (Williams-Stroud et al., 2020). (b–c–d) Vertical cross-sections parallel to the elongation of clusters (b) C, (c) G and (d) D3. Maximum (Max) and minimum (Min) *b*-values are indicated for each cluster.

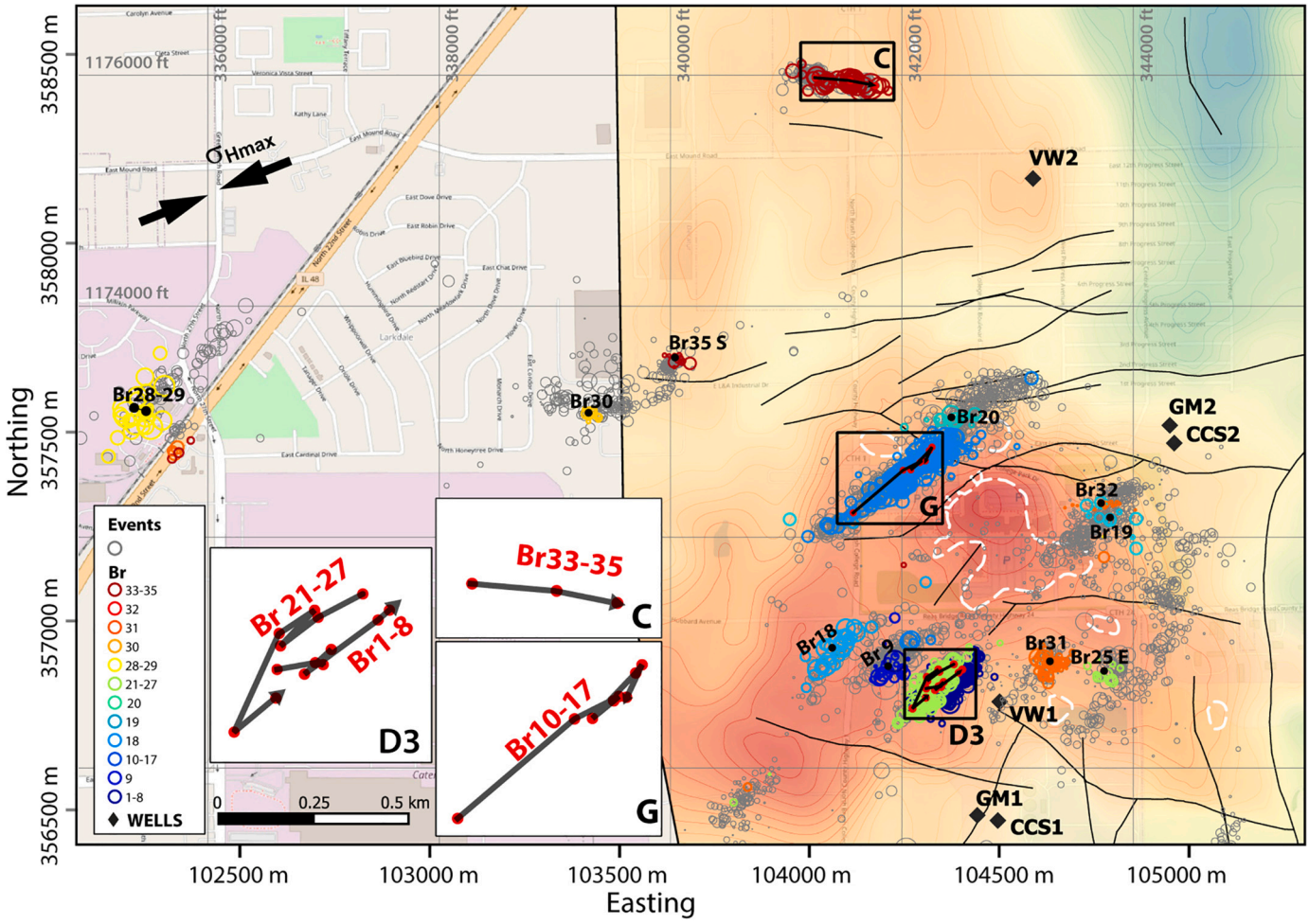

Fig. 7. Map illustrating distribution of bursts (colored circles) and their centroids (black dots). The centroids of consecutive bursts occurring within the same cluster are shown in the three figure insets (bottom left corner) by red dots and their temporal progression is highlighted by black arrows. Wells are shown by diamonds. Events that are not part of the cluster are marked by gray circles. For map location, see dashed rectangle in Fig. 1. Note that Br25 and Br35 are distributed over different clusters and therefore are also reported as Br25E (east) and Br35S (south). (For interpretation of the references to color in this figure legend, the reader is referred to the web version of this article.)

and D6 was therefore excluded from further analysis.

The overall geometry of D5 is similar to D1–D4 (Fig. 5) and it is aligned with D3. Between these clusters and cluster D5, two faults striking NE-SW and one striking E-W have been mapped in the sedimentary rocks overlying the basement. However, no seismicity is observed along these faults, and it is possible that they do not reach into the basement, where we observe events in D3 and D5. The southwestern terminations of clusters D1-D3 and D4 and D7 are located close to two WNW-ESE striking faults, that are potentially limiting seismicity or truncating the structures exhibiting seismicity, thus most likely reaching hypocentral depth.

Well VW1 is located in the vicinity of cluster D4 (Fig. 5a) allowing a direct comparison of the cluster strike to fractures intersected by the well at basement depth as interpreted on FMI (see rose diagram in Fig. 5c, top left). Four main fracture sets have been recognized in VW1 at basement depth, striking NE-SW, E-W, N-S, and NW-SE. The strike of cluster D4, and similarly D1-D3, D5, and D7, are in good agreement with the NE-SW set of open bed-bounded or open continuous fractures. Clusters of seismicity were not observed to form parallel to the E-W, N-S and NW-SE striking sets of fractures. In addition, two main sets of fractures were interpreted above the basement, striking NNE-SSW to NE-SW and NW-SE. Additionally, 16 focal mechanisms have been computed using first-motion P-wave polarities for clusters D4, D5, and D7 (Fig. 5a) following the computational method by Langet et al. (2020) and, given the overall orientation of the cluster they belong to, they consistently suggest a dextral strike-slip mechanism on NE-striking fault planes. Two events in cluster D5 feature a strike-slip mechanism as well, but on E-W striking fault planes, highly similar to the focal mechanisms computed for cluster C, suggesting that they might be caused by structures similarly oriented to cluster C.

The *b*-values for cluster D3 (Fig. 6a) decrease along the strike with the highest value at the southwesternmost tip. The events to the southwest are also located at shallower depth compared to the events located to the northeast (Fig. 6c), indicating that the relative size of the events, and therefore the slip area, generally increases with depth.

4.1.2. *Cluster G*

Cluster G is located north of clusters D1–D7 (Fig. 5) and has a NE-SW overall orientation in map view. The northernmost limit of this cluster is sharp and rotated closer to E-W, consistent with one of the faults mapped in the sedimentary rocks overlying the basement and extended downward to the top of the basement (black lines in Fig. 5).

Based on microseismicity, the cluster is highly linear south of 357,500 m Northing and slightly curved north of it (yellow dashed line in Fig. 5) and, an E-W, but locally NW-SE, striking fault interpreted from the 3D seismic data, separates the region to the NE from the region to the SW. The cluster is located between a topographic basement high to the south and topographic low to the north with elevation differences of

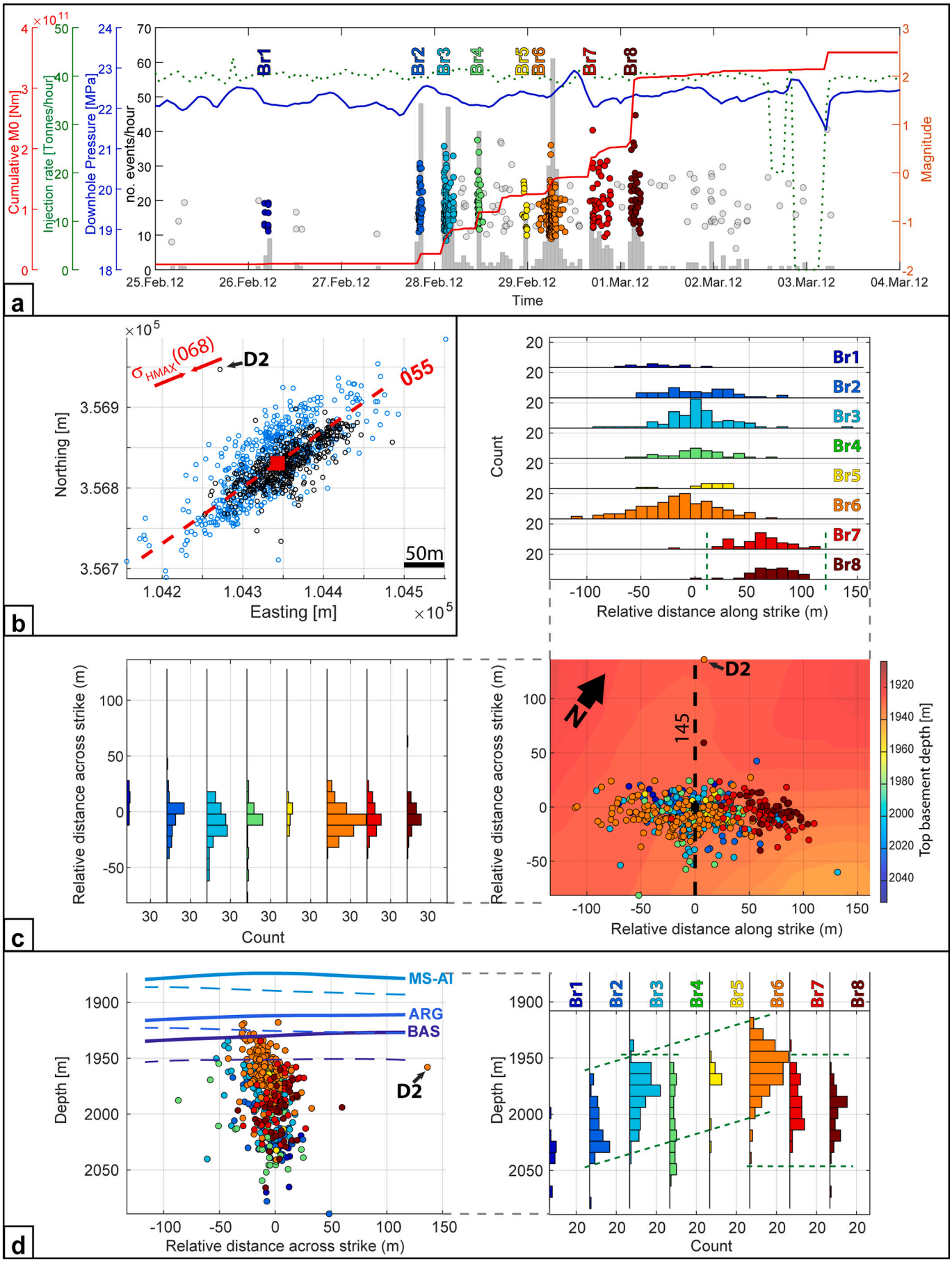

(caption on next page)

Fig. 8. Overview of bursts 1 to 8 within cluster D3. (a) Time vs. magnitude and histogram plots of the number of events for the period between February 25 and March 4, 2012. The eight bursts are shown as colored dots (from blue to dark red). Cumulative seismic moment (M0), injection rate, and downhole pressure are illustrated by the red, green, and blue curves, respectively. Remaining events are displayed as gray dots. (b) Map-view of cluster D3 (light blue dots) and the bursts 1–8 (black dots) together with the linear best-fit (red dashed line) and the cluster's centroid (red square). Maximum horizontal stress average orientation is indicated by red arrows. (c) Rotated map-view (background: Top of basement depth) and histograms parallel and orthogonal to the linear best fit strike of cluster D3. (d) Cross-section view along the dashed line shown in c) and corresponding depth histogram. Top of the basement (BAS), Argenta formation (ARG), and Mt. Simon unit A (MtA1) indicated as extracted from the reprocessed seismic volume (solid curves) and the earlier seismic volume (dashed lines). Green dashed lines support interpretation (see text). (For interpretation of the references to color in this figure legend, the reader is referred to the web version of this article.)

approx. 60 m (Fig. 5). The events to the northeast are located comparably deeper in elevation, migrating downdip along the topography of the Precambrian.

The *b*-values for cluster G (Fig. 6) show variability along strike. The shallower events occurring on the southwesternmost tip are characterized by higher *b*-values while the deeper events occurring on the northeasternmost tip display lower *b*-values. This variation in *b*-value indicates that the relative size of the events, and therefore the slip area, generally increases with depth, similar to what we observe for D3. However, the change in *b*-values along strike for G is less gradual suggesting a larger structural complexity of this cluster compared to D3 or the interaction of cluster G with other structures. The lowest *b*-values are concentrated in the region north of 357,500 m Northing, between two E-W striking faults.

4.1.3. Cluster C

Cluster C has a strike of ca. 102° and an elongation of approx. 340 m. Centroid depth of this cluster is larger compared to clusters in region D (see Table 1), corresponding to the lower elevation for the top of the basement (Fig. 5).

VW2 is located approximately 500 m ESE of cluster C and two main fracture sets striking E-W to ESE-WNW and NNW-SSE to NW-SE were interpreted on FMI at this well at basement depths (see rose diagram in Fig. 5c, bottom left). The first set is consistent with the overall orientation of cluster C and with a fault trace interpreted in the sedimentary rocks overlying the basement, just south of the cluster. Fractures belonging to both of these sets were classified as open continuous or open bed-bounded. Fractures interpreted above the basement are NNW-SSE striking and mainly open bed-bounded. A fault intercepted by the well is oriented ENE-WSW. Freiburg et al. (2020) observed two sets of discontinuities across the upper part of the basement in the early processed seismic attribute cube: (i) NNW-SSE striking discontinuities, similar in orientation to the structural trend in the basement topography to the east and north of VW2 interpreted on the reprocessed active seismic data (Fig. 1) and one of the fracture sets observed in the FMI of VW2, and (ii) ENE-WSW striking discontinuities, similarly oriented to the faults across the basement low and healed fractures interpreted above the basement on the FMI of VW2 (Fig. 5c, bottom left). The latter was not recognized as one of the main sets in the FMI at basement depth.

Furthermore, 23 focal mechanisms were computed for this cluster by Langet et al. (2020) and interpreted as sinistral strike-slip mechanisms on the slightly S of E and N of W oriented focal planes, consistent with both the overall 102° orientation of the cluster in map-view and the known stress field.

The *b*-values for cluster C display a similar pattern to the other analyzed clusters D3 and G, events to the west show higher *b*-values compared to the events to the east. Furthermore, events to the west, which have larger hypocentral variability compared to the east, show higher *b*-values compared to deeper events. Therefore, this cluster also suggests that the relative size of the events, and therefore the slip area, generally increases with the increasing depth of the events. Because of the overall fewer events in this cluster and larger distances between the events compared to clusters D3 and G, the *b*-value variability is the least gradual with discrete part of the cluster displaying relative similar *b*-values. However, note that cluster C does not include many events and the standard deviation of these *b*-value estimates is much larger compared to the other analyzed clusters (Goertz-Allmann et al., 2021).

4.2. Spatio-temporal evolution of bursts and other patterns

Overall none of the clusters have identified faults mapped with the seismic reprocessing (Fig. 5). Bursts and their structure are used to investigate possible structure internal to the clusters. An overview of the temporal evolution and location of the 35 recognized bursts is shown in Fig. 7. There is not a clear one-directional progression of the bursts with time, although bursts 1 to 17 occur in three clusters (D3, D2 and G), which are at increasing distance from the injection point. Consecutive bursts belonging to clusters D3 and G (e.g., Br1 to Br8 and Br10 to Br17), display general NE-alignments of the burst centroids (insets of Fig. 7).

In this section, consecutive bursts occurring in the three clusters D3, G, and C are analyzed. A majority of events in these clusters are well-located with low location uncertainties (average uncertainties of 2.6, 6.4 and 2 m in the East, North and Depth directions), achieved through event relocation (see Fig. 1). Seismic events need to be analyzed in 4D to extract as much information as possible and, if the objective is to geometrically define underlying structures, views parallel and orthogonal to the linear best fit strike of the event cluster are highly beneficial. They allow to minimize apparent geometries and angles (e.g., real vs. apparent dip) for the clusters, simplifying the analysis of possible differences in orientation of bursts and clusters. To investigate the burst sequences in 4D, we construct composite figures (Figs. 8–11) that allow us: (i) to investigate faults defined by the spatial distribution of events both, along strike and dip, (ii) to display spatio-temporal patterns and (iii) to identify smaller structures that might be oriented differently to the cluster or parts of the fracture being reactivated at different stages.

4.2.1. Cluster D3: Bursts 1 to 8 and Bursts 21 to 27

The first burst (Br1) occurred on February 26, 2012 (at 04:08:20 UTC), 2 days before the subsequent bursts (Br2 to Br8) took place within a period of less than 3 days (Fig. 8a). There is no clear correlation recognizable with injection rate or downhole pressure. The largest number of events occur in Br6 (141 events), however, the largest cumulative seismic moment (M0) is observed for Br7 and Br8.

These bursts occur in cluster D3 (with exception of one event, outlier in D2) which has overall elongation in direction 055° (Fig. 8b).

The rotated map-view parallel to the cluster strike (Fig. 8c) and its orthogonal cross-section (Fig. 8d) are accompanied by histograms showing the distribution and number of events along and across the burst cloud. Histograms displaying the distribution of events with local Northing (Fig. 8c, left) show a relatively homogeneous distribution of events, suggesting that each burst is oriented similarly to the entirety of bursts, while the histograms oriented along local Easting (Fig. 8c top) reveal that Br7 and Br8 occur at the NE-termination of the cluster. This may indicate an expansion of the seismic cloud due to stress perturbations caused by earlier burst events (Br1-Br6) at the tip of the slipping fault.

The depth distribution of burst events in cluster D3 shows that events are mostly located below the top of the basement with few events in the Argenta formation (Fig. 8d, left). The depth histograms indicate that bursts Br1-Br6 migrated upwards (Fig. 8d, right). Particularly Br2, Br3, and Br6 show a similar geometry (strike and dip in Table 2). Although the overall cloud of events can be interpreted as a near-vertical structure, single bursts are steeply dipping to the NW (between 70° and 55°) and could represent discrete slip-planes. It is interesting to note that the observed migration pattern of bursts is opposite to the overall migration

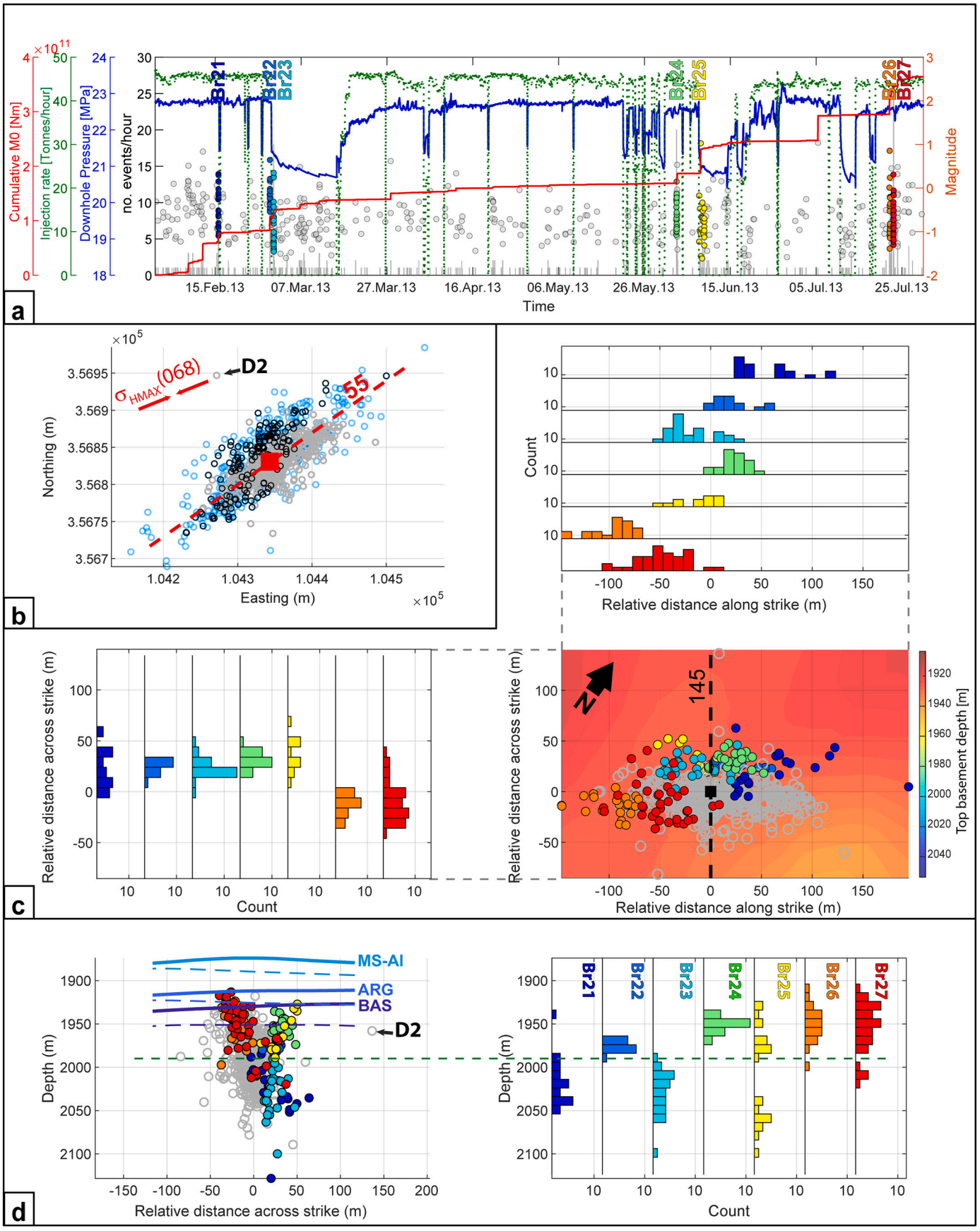

(caption on next page)

Fig. 9. Overview of bursts 21 to 27 within cluster D3. (a) Time vs. magnitude scatter and histogram of the number of events between February 1 and July 30, 2013. The seven bursts are shown as colored dots (from blue to dark red). Cumulative seismic moment (M0), injection rate, and downhole pressure are shown by the red, green, and blue curves, respectively. (b) Map-view of cluster D3 (light blue dots), Br1-Br8 (gray dots) and Br21-Br27 (black dots) with the linear best fit strike of cluster D3 (red dashed line) and the cluster centroid (red square). Maximum horizontal stress average orientation is also shown (red arrows). (c) Rotated map-view around the cluster centroid of the seven bursts and histograms (top) parallel and (bottom) orthogonal to the linear best fit strike of cluster D3. (d) Cross-section view along the dashed line shown in c, and corresponding depth histogram. Top of the basement (BAS), Argenta formation (ARG), and Mt. Simon unit A (MS-A1) are shown as solid lines for the reprocessed seismic volume and as dashed lines for the early seismic volume. Gray dots are the early bursts Br1–8 as described in Fig. 8. Top of the basement map is shown in the map-view in c. Green dashed lines support interpretation (see text). (For interpretation of the references to color in this figure legend, the reader is referred to the web version of this article.)

pattern of events within cluster G and C as observed by Goertz-Allmann et al. (2017).

One year after Br8, seven bursts (Br21–27) reappear in cluster D3 (Fig. 9a), following bursts in cluster D2 and G. The first of these bursts occurs on February 15, 2013 (Br21) and the last on July 23, 2013 (Br27). Three injection shut-ins occur during the same period. Some bursts appear to align with injection shut-ins in Fig. 9a). This is a visual artifact of the compressed *x*-axis. Br22 and Br24 occurred during many days of stable injection and hours before any shut-in. B23 and Br25 occur at varying times into a shut-in alongside Br22 and Br24, respectively. No consistent correlation is observed with injection rates, pressure changes, pressure change with injection time length or time intervals after injection start-up or shut-in. A number of events of Br25 is distributed in cluster D7, therefore, we reported these events as Br25E (east) (see Table 2 and Fig. 7). The event centroids of Br25 and Br25E (see Fig. 7) are located at similar distance from CCS1 (411 m and 494 m, respectively).

In Fig. 9b and c, gray dots represent Br1 to Br8 and both these figures indicate that Br21–27 surround the earlier events, particularly in the NW and at the SW tip of the event cloud. This spatial distribution is also evident in the histograms in Fig. 9c. Furthermore, Br22–Br23 and Br26–Br27 are separated by a short time interval (Fig. 9a), suggesting that both bursts reactivate two patches of the same structure at different times.

The vertical cross-section orthogonal to the linear best fit strike of cluster D3 (Fig. 9d, left) illustrates that bursts Br21 and Br23 are located deeper, while the later bursts (Br24 to Br27) are located at shallower depth. Especially important is that, all events of Br22 are located at a similar depth. Br24 and Br25 seem also to deviate from the general cloud geometry, as they may together indicate a change in dip-direction above approximately 1980 m depth and potentially indicate of small conjugate fractures (Fig. 9d).

Later events (Br21–Br27) surrounding earlier events (Br1–Br8) suggest stress changes to the edge of the slip surfaces, caused by the slip on these early bursts, i.e. a possible observation of the Kaiser effect (Kaiser, 1950). It is interesting to note that earlier events (Br1-Br8) have a higher *b*-value of 0.98 compared to later events (Br21-Br27) with a *b*-value of 0.79, which indicates an overall increase in size and slip area.

4.2.2. Cluster G: Burst 10–17 and Burst 20

Br10 to Br17 occur in cluster G from June 15 to July 12, 2012 (south of 357,500 Northing; Fig. 10a; see also Fig. 7). Br11 to Br16 occur over the course of 3 days, 8 days after Br10. Br11 to Br13 seem to occur during a period of low injection rates just after a shut-in, although no obvious correlation of the downhole pressure with the burst activity is observed (Fig. 10a). Br17 occurs 14 days after Br16. Finally, Br20 occurs again in cluster G, but 155 days later and is plotted in Fig. 10c and d as black dots and histogram.

The linear best fit strike of cluster G is 054° (Fig. 10b). Few events of these bursts take place within clusters D3 and D2, where earlier bursts transpired. Br11 to Br16 bursts show less distinct separation in both time and space in comparison to Br1-Br8 (Fig. 2c). Events occur often at similar locations in map-view, but within different bursts (see histogram in Fig. 10c top). Although this recurrence of events at the same locations partially obscures patterns, linear structures can still be interpreted (green dashed lines in Fig. 10c) and may indicate sub-parallel weakness zones being reactivated simultaneously. Extracting strike and dip from the combined burst event locations does not provide accurate values, but we can infer that the azimuth orientation of these bursts is similar to Br20.

The first burst in cluster G (Br10) defines the southwesternmost tip of the cluster. These events are located within a narrow 20 m depth interval (between 1970 m and 1990 m BSL) and are aligned with the overall burst cloud (Fig. 10b–c). Later bursts (Br15 to Br17) occur slightly deeper than earlier bursts (Fig. 10d, right). The events of Br20 are also located within a narrow depth range, similar to Br10. Both these clusters might indicate layers characterized by depth-confined fractures.

All events (except one, potentially mislocated event) occur within the basement (Fig. 10c).

As shown in Fig. 6, cluster G is characterized by a higher *b*-value toward the SW-tip of the cluster (corresponding to events within Br10). Goertz-Allmann et al. (2021) suggest that these events, which are constrained to a relatively thin depth interval, may point to stratabound fractures being reactivated. Higher *b*-values represent a larger number of small magnitude events, which is consistent with stratabound fractures of limited vertical length and thus slip area.

4.2.3. Cluster C: Burst 33–35

Br33 to Br35 occur in the northernmost cluster C from August 24, 2014 to January 21, 2015 (Fig. 11a). The durations of Br33 and Br34 are 8 h 24 min and 13 h 56 min, respectively and Br35 takes place 131 days after Br34 during the PH1 shut-in and is the only burst during the shut-in. Outside of the permanent shut-in, one temporary shut-in is observed during this period, but again, does not seem to correlate with burst activity (Fig. 11a). The overall cloud of cluster C has an elongation in direction of 102° (Fig. 11b). A few events within Br33–Br35 appear in clusters A and B at rather far distances from cluster C and in the most populated areas within these clusters (see Fig. 1). Such multi-location bursts (see e.g., Br35 and Br35S in Fig. 7) could potentially indicate local pressure increase due to heterogeneities. Fig. 11c and d focus only on the events within cluster C, which reduces the number of events in each burst as listed in the legend in Fig. 11c top. A clear eastward migration of the burst seismicity is observed, similar to the entire cluster. Br34 and Br35 are located deeper than Br33 (see Fig 11d). The azimuth of bursts is similar to the cluster orientation (Fig. 11c, left) and the bursts delineate steeply dipping structures.

4.3. Clusters, bursts, and stress orientation

Burst orientation is generally consistent with the cluster orientation they belong to (compare Fig. 5b left and center). However, in cluster G, burst analysis in plan-view showed linear features at an angle to the cluster strike (green dashed lines in Fig. 5b center and Fig. 10c). Although these linear features are partially obscured by events occurring at the same location, their strike is similar to Br20. These features represent a series of sub-parallel fractures that get reactivated almost simultaneously during the bursts.

The interpreted planes defined by the extracted geometry (strike and dip) from clusters and bursts (Tables 1 and 2) allow us to investigate the likelihood of that these structures to being reactivated in the current stress regime, using slip-tendency analysis. Due to the recurrent seismicity and the modest pore pressure increase from the injection, the

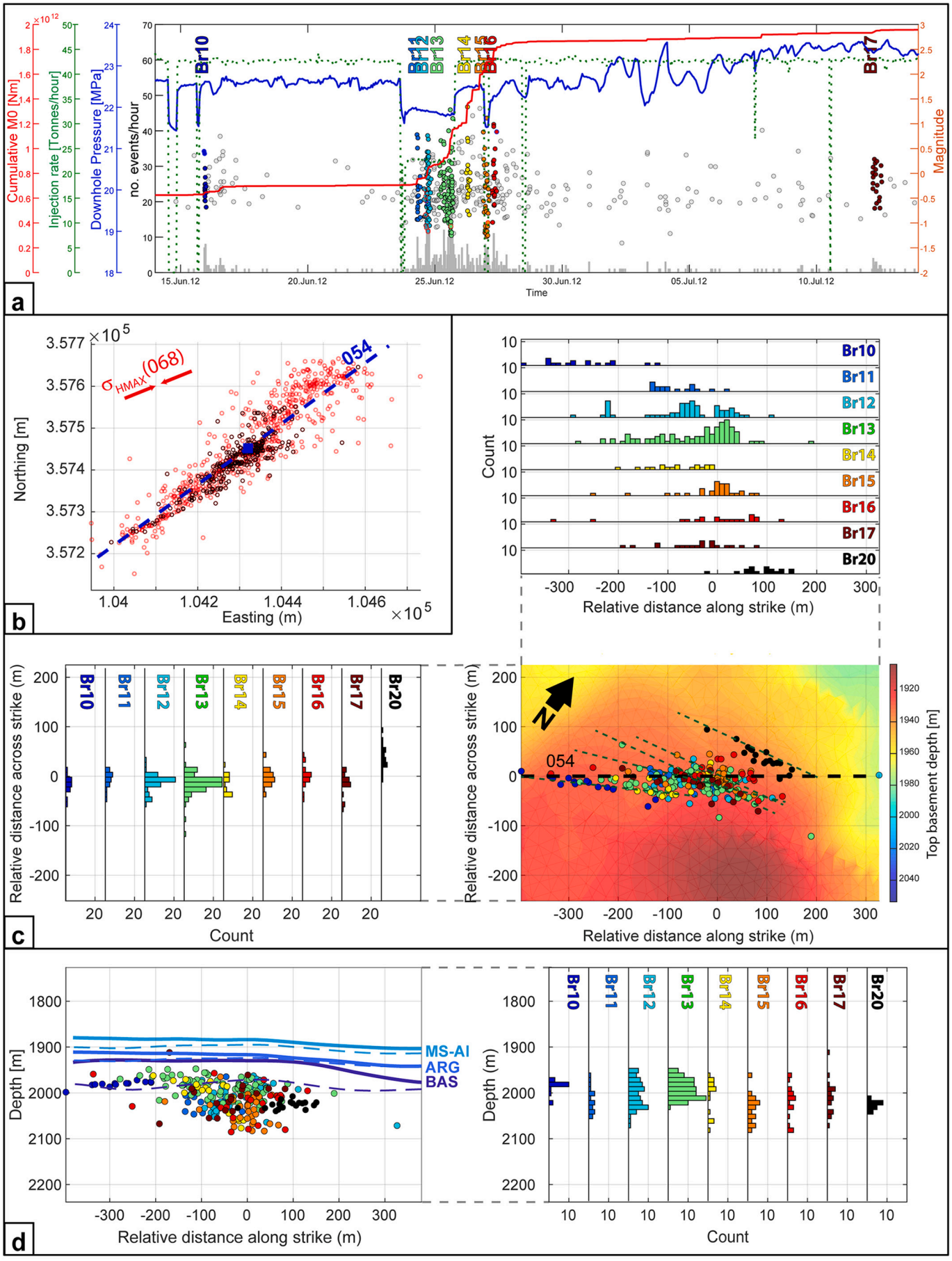

(caption on next page)

Fig. 10. Overview of bursts 10 to 17 (and Br20) within cluster G. (a) Time vs. magnitude scatter and histogram of the number of events for the period between June 14, 2012 and July 14, 2012. The eight bursts are shown as colored dots (from blue to dark red). Cumulative seismic moment (M0), injection rate, and downhole pressure are shown by the red, green, and blue curves, respectively. (b) Map-view of cluster G (red dots), showing the eight bursts Br10–17 and Br20 (black dots) and the linear fit (blue dashed line). Maximum horizontal stress average orientation is also shown (red arrows). (c) Rotated map-view parallel to the linear best fit strike of cluster G around the cluster centroid and rotated histograms. (d) Cross-section view along the dashed line shown in c, and relative depth histogram. Top of the basement (BAS), Argenta formation (ARG), and Mt. Simon unit A (MS-A1) are shown as solid curves for the reprocessed seismic volume and as dashed curves for the early seismic volume. Br20 is shown as black dots and histograms. Top of the basement map is shown in the map-view in c. (For interpretation of the references to color in this figure legend, the reader is referred to the web version of this article.)

planes extracted from clusters and bursts can be assumed to be optimally (max. slip tendency) to preferentially oriented (high slip tendency) to the stress field.

The tendency of a plane to slip (or slip tendency) in a given stress regime depends on the orientation and magnitude of the effective stresses acting on the fault surface and the friction coefficient of intact rock or pre-existing fracture or fault plane.

Slip tendency T_s [–] can be expressed as the ratio of shear stress to effective normal stress on a surface:

$$T_s = \frac{\tau}{\sigma_n'} \tag{1}$$

where τ [Pa] is the shear stress and $\sigma_n' = \sigma_n - P_f$ [Pa] is the effective normal stress acting on the fault/fracture plane, and P_f [Pa] is the pore pressure.

The stress regime at Decatur is characterized by high horizontal stress (σ_H), with an average azimuth of 068°, as measured at CCS1 and inferred from breakouts and drilling induced tensile failures in all the boreholes. Measurements in the Mt. Simon and Eau Claire formations indicate that the stress regime is strike-slip ($\sigma_H > \sigma_V > \sigma_h$) with most likely localized normal faulting ($\sigma_V > \sigma_H > \sigma_h$) for materials with low elastic moduli. Information extracted from the basement indicate also a strike-slip regime (Bauer et al., 2016) as well as the focal mechanisms for events in regions C and D which suggest that the dominant stress regime at the hypocentral depth (approximately 2.3 km TVD from ground level, within the basement) is strike-slip. Source mechanisms for larger earthquakes in other parts of Illinois and the surrounding area also are dominantly strike-slip (e.g., Lahann et al., 2017; Rupp et al., 2018). A range of stress magnitude gradients between 28.29 MPa/km and 43.11 MPa/km for the maximum principal σ_H, 24.48 MPa/km for the intermediate principal stress, and 24.48 MPa/km for the minimum principal stress has been measured at FutureGen (Cornet, 2014) and used in the slip tendency analysis. The three possible scenarios based on three different σ_H magnitudes for the strike-slip stress state are reported in Table 3.

The in situ hydrostatic gradient before injection derived from formation pore pressure monitoring was 10.3 MPa/km (Bauer et al., 2016) and was used to derive the principal effective stresses (Table 3). Pore pressure changes have not been included in the slip tendency analysis, since they are assumed to be small in the basement, where the seismicity is located.

The remaining unknown, needed for the slip tendency analysis, is the friction coefficient μ, which is typically between 0.55 and 0.85 (yellow region in Fig. 12a right). If we assume that the mobilized friction coefficient μ_m [–] (defined as the cohesionless Coulomb failure envelope for the current stress state) is equal to the friction coefficient of the small-scale optimally-oriented fractures that fail, producing microseismicity, we can derive μ_m as the tangent to the Mohr circle.

The following slip tendency analysis employs the stress state at a depth of 2100 m BSL (2307 m TVD from ground level), where most of the seismicity is centered. At this depth, the mobilized friction angles φ_m are between 19.85° and 35.01° for the three possible scenarios for the stress state (Table 3 and Fig. 12a, right). Note that the friction angle is $\arctan(\mu)$.

In general terms, within the same stress regime, large variations in maximum horizontal stress magnitude only slightly affect the orientation of fractures displaying the highest slip tendency (Fig. 12a left). On the other hand, a change in orientation (azimuth and plunge) of the principal stress axes is strictly linked to the orientation of fractures that are optimally oriented (e.g., within the 95%, full contours). A change in the azimuth of the principal stresses determines a change in the strike of optimally oriented fractures, while a change in the plunge of the minimum and intermediate principal stresses determines a change in their dip. Therefore, even for a hypothetical larger gradient for σ_H, all the planes of focal mechanisms will not display the highest (95%) slip tendency. However, Fig. 12a shows that for case 3 ($\sigma_H = 43.11$ MPa/km, Table 3 and Fig. 12), most of the focal mechanisms of region C lie within regions with the highest (95%) slip tendency, and therefore this value was used in the following analyses. The focal mechanisms were computed using an increment of 5°, which also corresponds to the accuracy of the focal plane orientation.

The orientation of clusters, bursts, and the fault planes from the focal mechanisms for region D, G and C are plotted on the slip tendency stereonets for a strike-slip regime with an average azimuth of 068° for σ_H (Fig. 12b), using FracTend (Healy, 2021). Most of the planes show a good agreement: NE-SW striking, mostly steeply dipping to the NW dominantly in regions D and G, while the closer to E-W orientations of 102° occur more in region C, mostly steeply dipping to the SSW. Because of the variability of the focal planes (Fig. 12b), we additionally plot the mean (MS) and the best solution (BS) for cluster C (as reported by Langet et al., 2020).

Both the slip tendency and the Mohr diagram (Fig. 12b bottom) suggest that cluster C, the E-W to ENE-WSW focal planes from focal mechanisms, and in general E-W to ENE-WSW striking fractures are optimally oriented to reactivation (>90%), while NNW-SSE to NW-SE striking fractures observed in the basement at VW2, as well as the structural trend in the basement topography similar to the set of discontinuities interpreted by Freiburg et al. (2020), both have the lowest slip tendency value (approx. 0.1, gray crosses in Fig. 12b bottom) and do not display seismicity.

In both regions D and G, the slip tendency and the Mohr diagram (Fig. 12b top and center) suggest that clusters, focal mechanisms and bursts are favourably oriented to slip, but plot at a small angle (up to ca. 10°) from the optimally oriented region for reactivation (>90%). N-S and NW-SE striking fractures measured at the VW1 have the lowest slip tendency value (approx. 0.1, gray crosses in Fig. 12b top and center), while E-W oriented faults are optimally oriented to slip, although only two focal mechanisms were observed in cluster D5 displaying this orientation.

In G, bursts are not optimally oriented, but this is expected since we observed that linear features were not properly captured by burst analysis and that they lie at an angle to cluster and burst orientation. The strike of these features is reported in the stereonet as green dots in Fig. 12b, Region G, center left, and they show generally higher slip tendency than the bursts in cluster G.

5. Discussion

When mapping the subsurface, detection of faults with active seismic imaging is often limited by the quality of the imaging and the wavelength such that faults with vertical displacement less than approx. 10 m are difficult to resolve at large depths. Microseismic monitoring can provide additional information about subseismic structures when

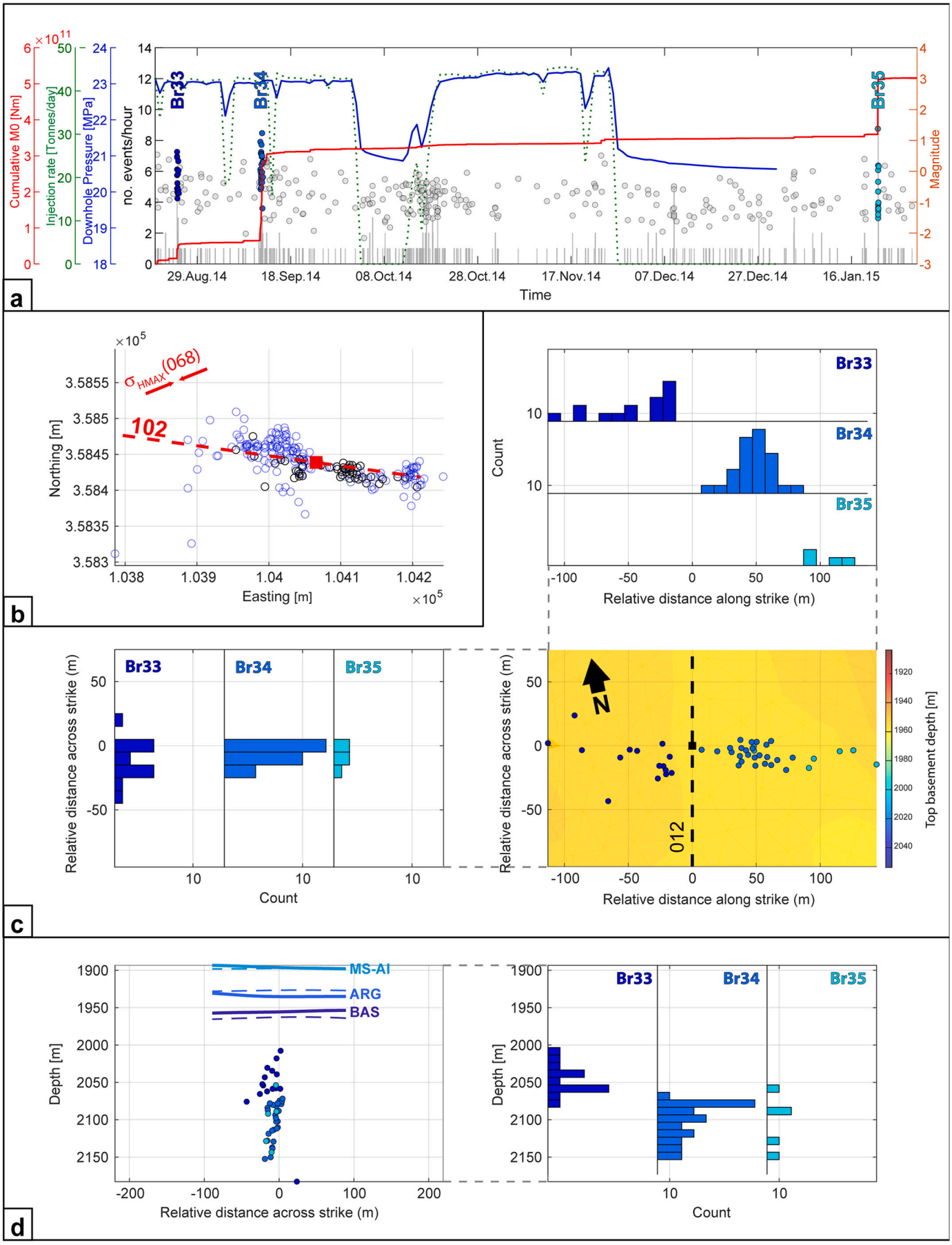

(caption on next page)

Fig. 11. Overview of bursts 33 to 35 within cluster C. (a) Time vs. magnitude scatter and histogram of the number of events for the period between August 20, 2014 and January 30, 2015. The three bursts are shown as colored dots (from blue to cyan). Cumulative seismic moment (M0), injection rate, and downhole pressure are shown by the red, green, and blue curves, respectively. (b) Map-view of cluster C (blue dots), and Br33 to Br35 as black dots, the cluster linear fit (red dashed line) and the cluster centroid (red square). Maximum horizontal stress average orientation is also shown (red arrows). (c) Rotated map-view of the three bursts and histograms parallel to the linear best-fit strike (relative distance across strike, left) and orthogonal to the linear best-fit strike (relative distance along strike, top) on the cluster. (d) Cross-section view along the dashed line shown in c, and relative depth histogram. Top of the basement (BAS), Argenta formation (ARG), and Mt. Simon unit A (MS-A1) are shown as solid curves for the reprocessed seismic volume and as dashed curves for the early seismic volume. Top of the basement map is shown in the map-view in c. (For interpretation of the references to color in this figure legend, the reader is referred to the web version of this article.)

Table 3
Three scenarios for a strike-slip stress regime. $\nabla\sigma_H$, $\nabla\sigma_V$ and $\nabla\sigma_h$ are the principal stress magnitude gradients; TVD [m] = true vertical depth from ground level; P_f [MPa] = pore pressure; $\sigma_H^{'}$[MPa], $\sigma_V^{'}$[MPa] and $\sigma_h^{'}$ [MPa] are the effective principal stress at the target depth; μ [–] and φ_m [°] are the friction coefficients and the frictional angles, respectively.

Case	$\nabla\sigma_H$ [MPa/km]	$\nabla\sigma_V$ [MPa/km]	$\nabla\sigma_h$ [MPa/km]	TVD [m]	P_f [MPa]	$\sigma_H^{'}$ [MPa]	$\sigma_V^{'}$[MPa]	$\sigma_h^{'}$ [MPa]	μ, μ_m [–]	φ_m, φ_m [°]
1	28.29	24.48	19.17	2307	23.8	41.50	32.71	20.46	0.55	28.81
									0.85	34.99
									0.35	19.85
2	35.7	24.48	19.17	2307	23.8	58.60	32.71	20.46	0.55	28.81
									0.85	34.99
									0.50	28.84
3	43.11	24.48	19.17	2307	23.8	39.9	33.7	20.1	0.55	28.81
									0.85	34.99
									0.61	35.01

induced seismicity denotes the reactivation of small-scale faults, allowing the identification of unresolved smaller-scale weakness zones or fractures or faults with predominant strike-slip motions. During injections conducted far below the expected fracture pressure of a formation, new fractures are unlikely to be created. However, pre-existing fractures and faults that are critically stressed and preferentially oriented can be reactivated by slightly elevated pore-pressures due to fluid injection. During Ph1 at Decatur, the maximum pore pressure increase due to injection was only 5.4% within the areas in which seismicity has been observed (as monitored 300 m from the injection well and 67 m above the basement) (Williams-Stroud et al., 2020), implying that there is no potential for nucleating new fractures (hydrofracturing). However, the pore pressure increase within the pressure plume has a much larger spatial extent than the actual CO_2 plume (both mainly contained within the reservoir), and this increase results in stress transfer, as demonstrated by the occurrence of microseismicity, that extends to an even larger area laterally and vertically.

The relocated events and the updated horizon interpretation of the reprocessed seismic data place more than 90% of the events within the basement. The porosity inversion of the reprocessed seismic data more clearly distinguished the top of the Argenta formation from the top of the basement, such that the basement surface was interpreted to be located up to 80 m shallower in areas to the west and northwest of CCS1 with respect to the previous interpretation (Williams-Stroud et al., 2020). The elevation differences due to the change in horizon interpretation are shown in the composite plots (Fig. 8d, left; Fig. 9d, left; Fig. 10d, left, and Fig. 11d, left). As already observed in the previous catalogue, most of the microseismicity occurred during Ph1 and is located within the basement (Fig. 2); only a few events close to VW1 and SE of CCS1 occurred within the reservoir. During Ph2, a similar pattern is observed, with most of the events located in the basement (Fig. 2a). Seismicity bursts start occurring after approx. 4 months from the start of the injection at CCS1 and a similarly long delay (or perhaps slightly longer) from the end of the Ph1, marks the end of the burst-like seismicity (magenta lines in Figs. 2b and 3b).

The general lack of significant impedance contrasts within the Precambrian igneous rocks hinders the interpretation of faults, especially in case of minor offset faults, like at Decatur. Therefore, faults that were identified in the overlying sedimentary rocks and extended into the basement primarily based on geological characteristics such as their trace lengths and displacement magnitude, and on indications of disruptions of the seismic character in the basement. This may contribute to the lack of correlation between the faults interpreted from the active seismic volume and the faults derived from the microseismic clusters.

Cluster and burst analyses provide information complementary to the seismic interpretation, since the clusters are not along imaged fault traces. The burst within the cluster(s) have slightly different orientations which can indicate the arrangement of smaller fractures, or provide information on their fracture attributes. For example, we interpreted the linear bursts in cluster G to indicate a zone of stratabound fractures, where horizontal lithological boundaries limit the vertical extent of fractures. Furthermore, an E-W striking fault appears to mark the end of cluster G, and a sinuous fault-trace appears to mark the end of the development of Cluster G as consecutive bursts (see Fig. 5). If we only take the results from the cluster analysis, for cluster G we can use the semi-linearity (in plan-view) of a single approx. 780 m long structure and assume, based on the typical length-displacement relationship (Kim and Sanderson, 2005), that the fault corresponding to cluster G should have a displacement that would be clearly visible within seismic resolution, assuming that this fault is not mostly strike-slip. Burst analysis suggests that this cluster is not one continuous structure, but is in fact composed of multiple sub-parallel weakness zones (Fig. 10c). These smaller structures suggest a shorter length of the slipping plane compared to a simplified interpretation based on the full extent of the cluster. Furthermore, interpreted stratabound fractures of Br10 and Br20 might indicate separate and distinct structures adjacent to cluster G. The spatial analysis of *b*-value yields higher values at the southwesternmost part of the cluster, at the location of Br10, supporting the presence of larger proportion of shorter fractures here, compared to the rest of the cluster, therefore supporting the hypothesis that cluster G is not indicative of one single continuous structure. Another interesting observation from burst analysis is the recurrence of bursts spatially close to earlier bursts within the same cluster (in particular Br1–Br8 and Br21–Br27). The slip on earlier bursts might have caused stress changes on the rim of the slip surfaces, where the later bursts took place, i.e. an observation of the Kaiser or stress memory effect. This phenomenon describes that during re-loading, the seismicity only occurs at the margin of areas having been active earlier, as long as the stress level is below the one exerted during previous loading cycles (Kaiser, 1950; Lavrov, 2003). Earlier events display a higher *b*-value compared to later events

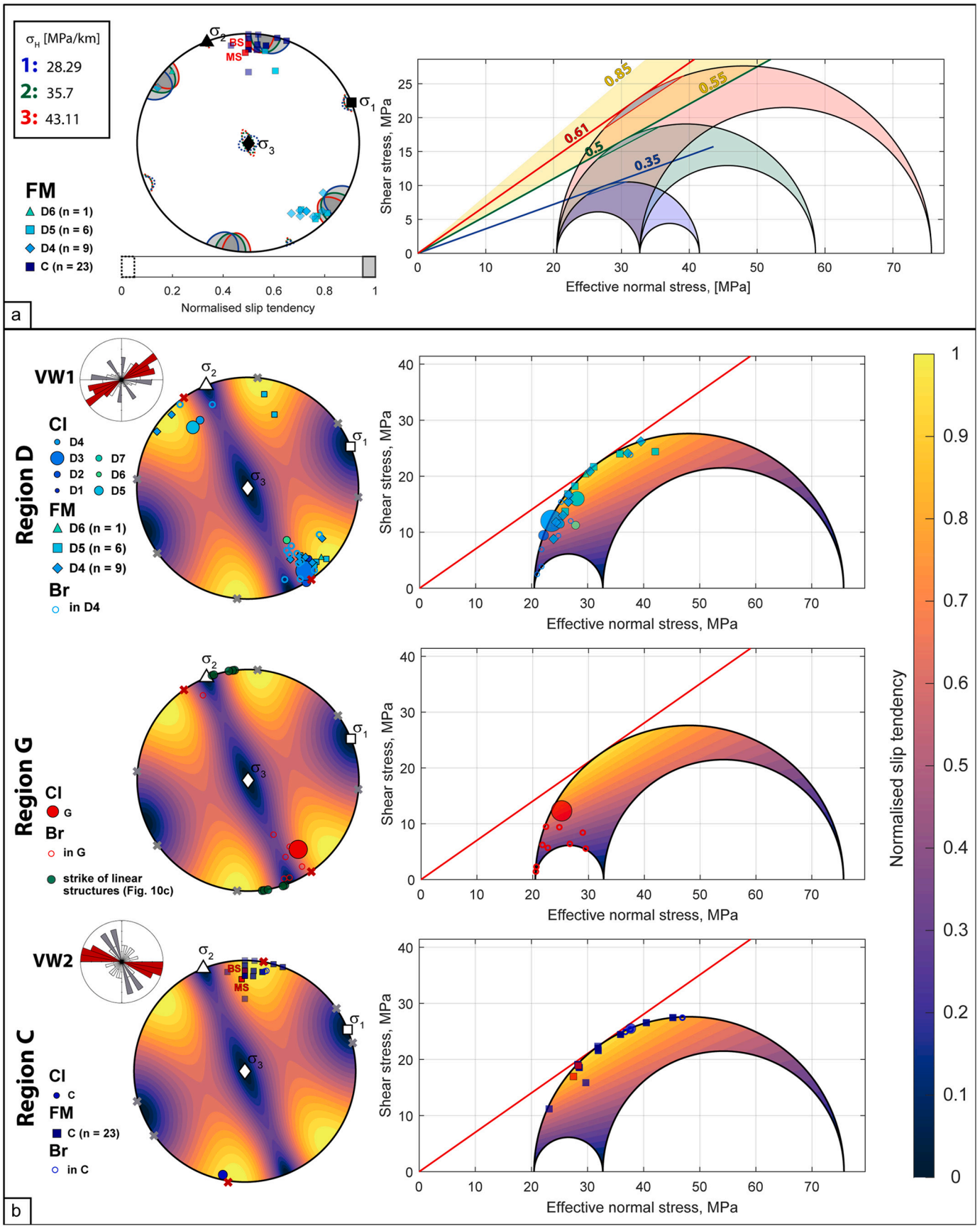

(caption on next page)

Fig. 12. (a) The stress states for the minimum (28.29 MPa/km), average (35.7 MPa/km) and maximum (43.11 MPa/km) gradients for the maximum horizontal stress shown in Fig. 3b and reported in Table 3 are shown on (left) an equal area stereonet and (right) a Mohr diagram. The corresponding regions with highest (95%, full contours) and minimum (5%, dashed contours) slip tendency for the three stress states are also indicated by the respective colors on the stereonet. The mobilized friction coefficient (0.35, 0.5 and 0.61) relative to each case are indicated on the Mohr diagram and reported in Table 3. Typical friction coefficient values (0.55–0.75) are indicated by the yellow region. The interpreted causative planes from focal mechanisms (FM) for clusters C, D4, D5, and D6 are plotted as poles to planes (see legend for symbols). (b) Slip tendency shown on (left) equal area lower hemisphere stereonets and (right) the Mohr's circle for a strike-slip regime with an average azimuth of 068° for the maximum horizontal stress, for regions (top) D, (middle) G and (bottom) C. Poles to fracture planes are plotted for: clusters (Cl), bursts (Br) and focal mechanisms (FM) (see legend for symbols). For cluster G, the strike of interpreted linear structures are represented by green dots. On the stereonets, the azimuth of major sets of fractures intercepted by VW1 and VW2 in the basement are represented by crosses color coordinated with the rose diagram insets, red for azimuth similar to observed seismicity, gray for other azimuths. MS = mean fit of FMs for cluster C; and BS = best fit of FMs for cluster C. (For interpretation of the references to color in this figure legend, the reader is referred to the web version of this article.)

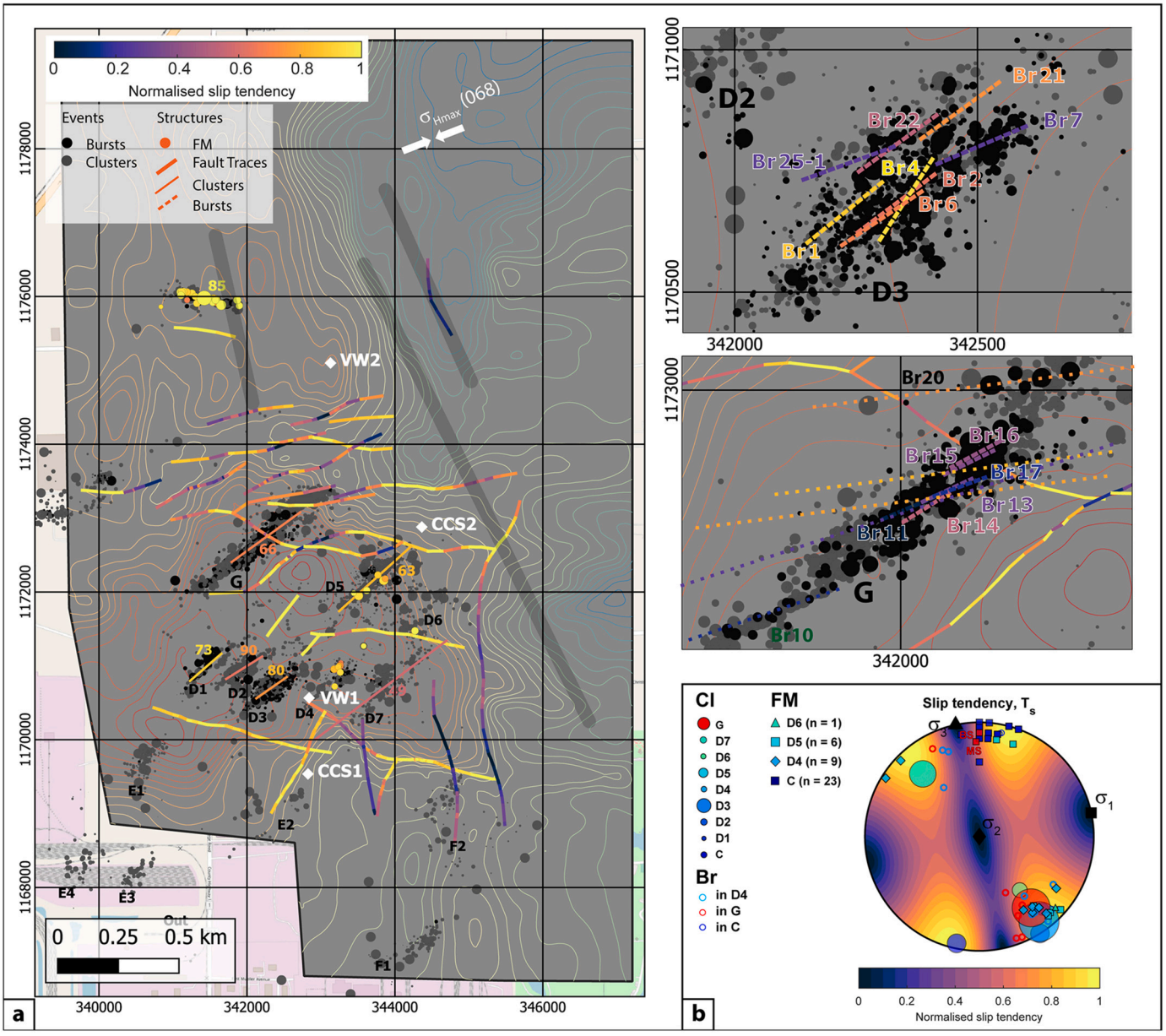

Fig. 13. (a) Map showing the top of basement topography, the interpreted fault traces from the newly reprocessed seismic volume at the depth of the top of the basement, cluster events (gray dots), burst events (black dots) and focal mechanisms (filled circles). Fault traces, reliable interpreted geometries from cluster analysis and focal mechanisms (dots) are colored by slip tendency for a maximum horizontal stress azimuth of 068° for the stress magnitudes discussed in Section 5. Labels are the dip of the planes extracted from the clusters and used in the slip tendency. Thick semi-transparent lines represent the approximate location of the NNW-SSE striking discontinuities observed by Freiburg et al. (2020). Two close-up figures for cluster D3 and G show the reliably interpreted geometries from burst analysis (dashed lines), and the linear features discussed in the text for cluster G, colored by slip tendency. (b) Slip tendency shown on equal area lower hemisphere stereonet for a strike-slip regime with an azimuth of 078°. Poles to fracture planes are plotted for: clusters (Cl), bursts (Br) and focal mechanisms (FM) (see legend for symbols). (For interpretation of the references to color in this figure legend, the reader is referred to the web version of this article.)

indicating overall larger events developing along growing fractures with time or the infiltration of fluid and pressure through early bursts that after slip, act as pathways. Last, the methodology used to select bursts from the catalogue allowed us to analyze if bursts occurring simultaneously at different locations may be indicative of similar pressure front conditions. This is for example the case of Br25 and Br25E, which are located at similar distances from the injection point. However, this was a single observation and a link to a defined pressure associated with the front would be highly speculative.

The slip tendency analysis of the strike orientation of the sub-vertical faults interpreted from active seismic data shows that in the defined stress regime (case 3 in Table 3), the N-S striking fault sets are not prone to reactivation, while the NE-SW and part of the E-W to WNW-ESE striking sets are optimally oriented for reactivation (thicker colored lines in Fig. 13a). However, these optimally oriented structures are not associated with the recorded microseismicity in region D and along the E-W basement low, centered approx. around 357,800 m Northing. This may suggest that these faults do not extend in the basement or that they are stronger (e.g., higher friction coefficients and cohesion) compared to the faults that display seismicity, which are not found on the active seismic interpretation. For instance, the fault south of clusters D1-D3 and, D4 and D7 could be limiting the seismicity (see Fig. 4), suggesting that it might extend down to hypocentral depth while not displaying seismicity despite its high slip tendency.

The slip tendency explains the seismicity of the northernmost cluster (C), which is optimally oriented under the stress regime (case 3, azimuth of $\sigma_H = 068^\circ$ and $\nabla\sigma_H = 43.11$ MPa/km), as well as the interpreted fault planes from focal mechanisms for this cluster (thin line and dots in Fig. 13a, respectively). On the other hand, clusters in region G and D, as well as, the NE-SW striking fault planes from focal mechanisms in region D (thin lines and dots in Fig. 13a, respectively) are not optimally but merely preferentially oriented. The few E-W striking structures identified in the area of cluster D5 are supported by burst analysis (Fig. 5) and two focal mechanism solutions (Fig. 1), both of which are optimally oriented under the well-documented stress regime.

Freiburg et al. (2020) suggested that the E-W basement low (Fig. 1), represents a lithological compartmentalization boundary for the basement (see Section 2). This may imply that pre-existing fractures are oriented differently north and south of it (as also suggested by the fractures intercepted by VW1 and VW2, Fig. 5c) or that the mobilized friction coefficients might vary between these two areas, or that both cases are present. Optimally oriented fractures might not exist south of the basement low or have higher friction coefficients that impedes their slip; if this is the case, fractures that lie at a small angle to the optimally oriented fractures might be reactivated instead, if their friction coefficient is lower than the ones of the optimally oriented fractures.

We observed that a slight deviation (clockwise rotation) of the maximum horizontal stress azimuth of approx. 10° from the average azimuth (068°) would have the NE-SW striking planes defined by the seismic clusters in region D closer to optimal orientation (Fig. 13b). In this hypothetical stress state, ENE-WSW striking structures along the basement low and N-S to NNW-SSE striking structures are not prone to reactivation, consistently with the lack of seismicity along this trend. This maximum horizontal stress orientation merely based on slip tendency analysis is within the spread of the azimuth of the drilling-induced maximum stress direction indicators and rather similar to the stress indicators from tensile induced fracture at the VW1 in the basement (Fig. 5b), thus it allows for an independent constrain of the maximum horizontal stress azimuth in region D, within the basement.

NNW-SSE striking fractures that were observed in VW2 as open fractures above and in the basement (Fig. 5c) have the same strike as linear topographic features on the top of the basement (Fig. 13a), and in the same location as one of the discontinuity trends interpret by Freiburg et al. (2020), Fig. 13. In particular, one of the discontinuities interpreted by Freiburg et al. (2020) occurs at the westernmost tip of cluster C (thick gray line in Fig. 13a). Since structures with this orientation are not preferentially oriented to slip, it may extend to focal depth and represent a barrier to further extension eastward of the cluster. The strike of these discontinuities is similar to the orientation of the Charleston monocline located approx. 45 km west of the Decatur site (Fig. 3). We speculate that these discontinuities observed at Decatur might have been caused by far-field stresses related to the same tectonic event.

The analysis of bursts allows us also to investigate the time progression of seismicity. At early stages of the injection, bursts occur progressively on clusters that are further away from the injection well (Br1–Br17), but this is not the case for later stages (Br18–Br35, Fig. 7). However, although the microseismicity is clearly triggered by the injection, no direct link could be established between burst initiations and either startup of injection periods or shut-ins. Therefore, the mobilized friction coefficient can be assumed to be close to the Coulomb failure envelope, which means that the basement is critically stressed.

Last, we demonstrate that the three scenarios for the stress regime (Table 3) lead to very small changes in the strike of fractures for optimal orientation to slip (Fig. 12a), which alone cannot explain the different orientation of clusters north and south of the basement low.

6. Conclusions

In this paper, we demonstrated that microseismicity complements active seismic data, particularly when seismic reflection imaging is either not of adequate resolution or when faults do not have sufficient vertical offset to be identified with confidence. Cluster and burst analyses contribute to the understanding of the geometry of pre-existing structures and their spatial arrangement with different levels of detail. This has important implications for the use of scaling relationship to estimate fracture size and expected event magnitudes.

At Decatur, a large majority of events occurs in the basement. Since faults interpreted from the active seismic data were extended from the overlying sedimentary rocks into the basement where fault indicators in the seismic imagery were more uncertain, they in practice might not necessarily reach the depth of the events. However, in cases that the lateral extent of clusters seems to be bound by interpreted mapped faults, it is possible that these faults do extend to the basement and acted as barriers to the extent of the structures illuminated by microseismicity.

In particular, we showed:

- Cluster analysis allows definition of the overall orientation and shape of the structures. Furthermore, the large amount of events allows for a reliable extraction of statistical parameters (related to the geometry of the seismic cloud).

- Bursts of seismicity are often concentrated in space and therefore resolve small-scale structures within the individual clusters. Multiple bursts within the same cluster indicate either slip on separate fault surfaces or partial slip on patches of a larger structure, that might be evidence of stress transfer or slightly different orientations than cluster orientation (e.g., en echelon faults).

- Cluster and burst analyses, *b*-values and focal mechanisms are independent analyses and their integration assures their mutual interpretations. For example, the geometry of the clusters allows to discriminate between the focal plane and auxiliary plane when interpreting focal mechanisms, and the inferences on fracture size from burst analysis due to confined event location is consistent with interpreted fracture size from *b*-value analysis.

Finally, we show that a slip tendency analysis of faults interpreted from the active seismic data, clusters and bursts, integrated with focal mechanisms, can provide insight about slight local deviations of the maximum horizontal stress azimuth from the average direction, lack of optimally oriented fractures in certain regions or suggest variability in the friction coefficient for differently oriented structures.

Declaration of Competing Interest

The authors declare that they have no known competing financial

interests or personal relationships that could have appeared to influence the work reported in this paper.

Acknowledgments

We are grateful for support through the Norwegian Climit programme of Gassnova, project number 618233. Data are provided by the Midwest Geological Sequestration Consortium (MGSC). MGSC is funded by the U.S. Department of Energy through the National Energy Technology Laboratory (NETL) via the Regional Carbon Sequestration Partnership Program (contract number DE-FC26-05NT42588) and by a cost share agreement with the Illinois Department of Commerce and Economic Opportunity, Office of Coal Development through the Illinois Clean Coal Institute. We are also grateful for the positive feedback and constructive reviews provided by Adam Baig and an anonymous reviewer that helped to improved the clarity of the manuscript.

Appendix A. Supplementary data

Supplementary data to this article can be found online at https://doi.org/10.1016/j.tecto.2021.229107.

References

Bauer, R.A., Carney, M., Finley, R.J., 2016. Overview of microseismic response to CO_2 injection into the Mt. Simon saline reservoir at the Illinois Basin-Decatur. Int. J. Greenh. Gas Control 54, 378–388. https://doi.org/10.1016/j.ijggc.2015.12.015.

Bauer, R.A., Will, R., Greenberg, S.E., Whittaker, S.G., 2019. Illinois Basin-Decatur. Geophysics and Geosequestration. Cambridge University Press, pp. 339–370. https://doi.org/10.1017/9781316480724.020.

Cornet, F., 2014. Results from the in-situ Stress Characterization Program; Phase 1: Geomechnical Tests Conducted in The FutureGen Stratigraphic Well (FGA# 1) PNWD-4421/FG-02-RPT-0009, p. 78.

Dando, B.D.E., Goertz-Allmann, B.P., Kühn, D., Langet, N., Dichiarante, A.M., Oye, V., 2021. Relocating microseismicity from downhole monitoring of the Decatur CCS site using a modified double-difference algorithm. Geophys. J. Int. 227 (2), 1094–1122. https://doi.org/10.1093/gji/ggab255.

Duboeuf, L., Dichiarante, A.M., Oye, V., 2021. Interplay of large-scale tectonic deformation and local fluid injection investigated through seismicity patterns at the Reykjanes Geothermal Field, Iceland. Geophys. J. Int. In press.

Finley, R.J., 2014. An overview of the Illinois Basin-Decatur project. Greenh. Gases Sci. Technol. 4 (5), 571–579. https://doi.org/10.1002/ghg.1433.

Freiburg, J.T., McBride, J.H., Malone, D.H., Leetaru, H.E., 2020. Petrology, geochronology, and geophysical characterization of Mesoproterozoic rocks in central Illinois, USA. Geosci. Front. 11 (2), 581–596. https://doi.org/10.1016/j.gsf.2019.07.004.

Freiburg, J.T., Morse, D.G., Leetaru, H.E., Hoss, R.P., Yan, Q., 2014. A Depositional and Diagenetic Characterization of the Mt. Simon Sandstone at the Illinois Basin – Decatur Project Carbon Capture and Storage Site. Illinois State Geological Survey Circular, Decatur, IL, USA, p. 583.

Furre, A.-K., Eiken, O., Alnes, H., Vevatne, J.N., Kiær, A.F., 2017. 20 years of monitoring CO_2-injection at Sleipner. Energy Proc. 114, 3916–3926. https://doi.org/10.1016/j.egypro.2017.03.1523.

Goertz-Allmann, B., Gibbons, S., Oye, V., Bauer, R., Will, R., 2017. Characterization of induced seismicity patterns derived from internal structure in event clusters. J. Geophys. Res. Solid Earth 122 (5), 3875–3894. https://doi.org/10.1002/2016JB013731.

Goertz-Allmann, B., Dando, B.D.E., Langet, N., Dichiarante, A., Kühn, D., Oye, V., Jordan, M., Williams-Stroud, S., Bauer, R., Greenberg, S., 2021. Long-term seismic monitoring of reservoir dynamics at Decatur. In: GHGT-15 Proceedings.

Goertz-Allmann, B.P., Kü hn, D., Oye, V., Bohloli, B., Aker, E., 2014. Combining microseismic and geomechanical observations to interpret storage integrity at the in salah ccs site. Geophys. J. Int. 198 (1), 447–461. https://doi.org/10.1093/gji/ggu010.

Greenberg, S.E., 2020. 2020 An Assessment of Geological Carbon Sequestration Options in the Illinois Basin: Phase III Quarterly Progress Report, October 1 December 31. Illinois State Geological Survey. Tech. Rep.

Healy, D., 2021. FracTend. https://github.com/DaveHealy-Aberdeen/FracTend.

Healy, J., Rubey, W., Griggs, D., Raleigh, C., 1968. The Denver earthquakes. Science 161 (3848), 1301–1310. https://doi.org/10.1126/science.161.3848.1301.

Kaiser, J., 1950. Untersuchungen über das Auftreten von Gerä uschen beim Zugversuch. Technische Hochschule Mü nchen. Ph.D. Thesis.

Kim, Y.-S., Sanderson, D.J., 2005. The relationship between displacement and length of faults: a review. Earth-Sci. Rev. 68 (3–4), 317–334. https://doi.org/10.1016/j.earscirev.2004.06.003.

Kolata, D., Nelson, W., 1990. Chapter 18: Part I. Illinois Basin: Evolution Tectonic History of the Illinois Basin. AAPG Special Volumes, pp. 263–285. https://doi.org/10.1306/M51530C19.

Lahann, R.W., Rupp, J.A., Medina, C.R., Carlson, G., Johnson, K.M., 2017. State of stress in the Illinois Basin and constraints on inducing failure. Environ. Geosci. 24 (3), 123–150. https://doi.org/10.1306/eg.0206171600817004.

Langet, N., Goertz-Allmann, B., Oye, V., Bauer, R.A., Williams-Stroud, S., Dichiarante, A.M., Greenberg, S.E., 2020. Joint focal mechanism inversion using downhole and surface monitoring at the Decatur, Illinois, CO_2, injection site. Bull. Seismol. Soc. Am. 110 (5), 2168–2187. https://doi.org/10.1785/0120200075.

Lavrov, A., 2003. The kaiser effect in rocks: principles and stress estimation techniques. Int. J. Rock Mech. Min. Sci. 40 (2), 151–171. https://doi.org/10.1016/S1365-1609(02)00138-7.

Leetaru, H.E., Freiburg, J.T., 2014. Litho-facies and reservoir characterization of the Mt. Simon Sandstone at the Illinois Basin-Decatur. Greenh. Gases Sci. Technol. 4 (5), 580–595. https://doi.org/10.1002/ghg.1453.

Leetaru, H.E., McBride, J.H., 2009. Reservoir uncertainty, precambrian topography, and carbon sequestration in the Mt. Simon Sandstone, Illinois Basin. Environ. Geosci. 16 (4), 235–243. https://doi.org/10.1306/eg.04210909006.

McBride, J.H., 1997. Variable deep structure of a midcontinent fault and fold zone from seismic reflection: La Salle deformation belt, Illinois Basin. Geol. Soc. Am. Bull. 109 (11), 1502–1513. https://doi.org/10.1130/0016-7606(1997)109<1502:VDSOAM>2.3.CO;2.

McBride, J.H., Leetaru, H.E., Bauer, R.A., Tingey, B.E., Schmidt, S.E., 2007. Deep faulting and structural reactivation beneath the southern Illinois Basin. Precambrian Res. 157 (1–4), 289–313. https://doi.org/10.1016/j.precamres.2007.02.020.

Morrow, C.A., Kaven, J.O., Moore, D.E., Lockner, D.A., 2017. Physical Properties of Sidewall Cores From Decatur. US Department of the Interior US Geological Survey Open-file Repot 2017–1094, Illinois. https://doi.org/10.3133/ofr20171094.

Rupp, J.A., Letsinger, S.L., Carlson, G., 2018. Fault angle control on potential seismic slip in the Illinois Basin region. Seismol. Res. Lett. 89 (6), 2461–2472. https://doi.org/10.1785/0220180153.

Sibson, R.H., 1985. A note on fault reactivation. J. Struct. Geol. 7 (6), 751–754. https://doi.org/10.1016/0191-8141(85)90150-6.

Tuttle, M.P., Schweig, E.S., Sims, J.D., Lafferty, R.H., Wolf, L.W., Haynes, M.L., 2002. The earthquake potential of the New Madrid seismic zone. Bull. Seismol. Soc. Am. 92 (6), 2080–2089. https://doi.org/10.1785/0120010227.

Verdon, J.P., 2016. Using microseismic data recorded at the Weyburn CCS-EOR site to assess the likelihood of induced seismic activity. Int. J. Greenh. Gas Control 54, 421–428. https://doi.org/10.1016/j.ijggc.2016.03.018.

Verdon, J.P., Kendall, J.-M., White, D.J., Angus, D.A., Fisher, Q.J., Urbancic, T., 2010. Passive seismic monitoring of carbon dioxide storage at Weyburn. Lead. Edge 29 (2), 200–206. https://doi.org/10.1190/1.3304825.

Vidale, J.E., Shearer, P.M., 2006. A survey of 71 earthquake bursts across southern California: exploring the role of pore fluid pressure fluctuations and aseismic slip as drivers. J. Geophys. Res. Solid Earth 111 (B5). https://doi.org/10.1029/2005JB004034.

Vilarrasa, V., Silva, O., Carrera, J., Olivella, S., 2013. Liquid CO_2 injection for geological storage in deep saline aquifers. Int. J. Greenh. Gas Control 14, 84–96. https://doi.org/10.1016/j.ijggc.2013.01.015.

Will, R., Smith, V., Leetaru, H.E., Freiburg, J.T., Lee, D.W., 2014. Microseismic monitoring, event occurrence, and the relationship to subsurface geology. Energy Proc. 63, 4424–4436. https://doi.org/10.1016/j.egypro.2014.11.478.

Williams-Stroud, S., Bauer, R., Leetaru, H., Oye, V., Stanek, F., Greenberg, S., Langet, N., 2020. Analysis of microseismicity and reactivated fault size to assess the potential for felt events by CO_2 injection in the Illinois Basin. Bull. Seismol. Soc. Am. 110 (5), 2188–2204. https://doi.org/10.1785/0120200112.

Yang, X., Pavlis, G.L., Hamburger, M.W., Marshak, S., Gilbert, H., Rupp, J., Larson, T.H., Chen, C., Carpenter, N.S., 2017. Detailed crustal thickness variations beneath the Illinois Basin area: implications for crustal evolution of the midcontinent. J. Geophys. Res. Solid Earth 122 (8), 6323–6345. https://doi.org/10.1002/2017JB014150.

Zhang, R., Vasco, D., Daley, T.M., Harbert, W., 2015. Characterization of a fracture zone using seismic attributes at the In Salah CO_2 storage. Interpretation 3 (2). https://doi.org/10.1190/INT-2014-0141.1. SM37-SM46.

Zoback, M.D., Gorelick, S.M., 2012. Earthquake triggering and large-scale geologic storage of carbon dioxide. Proc. Natl. Acad. Sci. USA 109 (26), 10164–10168. https://doi.org/10.1073/pnas.1202473109.